

# Ionization Electron Signal Processing in Single Phase LArTPCs

## I. Algorithm Description and Quantitative Evaluation with MicroBooNE Simulation

---

### MicroBooNE Collaboration

C. Adams<sup>i</sup> R. An<sup>j</sup> J. Anthony<sup>c</sup> J. Asaadi<sup>aa</sup> M. Auger<sup>a</sup> L. Bagby<sup>h</sup> S. Balasubramanian<sup>ee</sup>  
B. Baller<sup>h</sup> C. Barnes<sup>p</sup> G. Barr<sup>s</sup> M. Bass<sup>s,b</sup> F. Bay<sup>bb</sup> A. Bhat<sup>x</sup> K. Bhattacharya<sup>t</sup> M. Bishai<sup>b</sup>  
A. Blake<sup>l</sup> T. Bolton<sup>k</sup> L. Camilleri<sup>g</sup> D. Caratelli<sup>g</sup> R. Castillo Fernandez<sup>h</sup> F. Cavanna<sup>h</sup> G. Cerati<sup>h</sup>  
H. Chen<sup>b</sup> Y. Chen<sup>a</sup> E. Church<sup>t</sup> D. Cianci<sup>g</sup> E. Cohen<sup>y</sup> G. H. Collin<sup>o</sup> J. M. Conrad<sup>o</sup> M. Convery<sup>w</sup>  
L. Cooper-Troendle<sup>ee</sup> J. I. Crespo-Anadón<sup>g</sup> M. Del Tutto<sup>s</sup> D. Devitt<sup>l</sup> A. Diaz<sup>o</sup> S. Dytman<sup>u</sup>  
B. Eberly<sup>w</sup> A. Ereditato<sup>a</sup> L. Escudero Sanchez<sup>c</sup> J. Esquivel<sup>x</sup> J. J. Evans<sup>n</sup> A. A. Fadeeva<sup>g</sup>  
B. T. Fleming<sup>ee</sup> W. Foreman<sup>d</sup> A. P. Furmanski<sup>n</sup> D. Garcia-Gamez<sup>n</sup> G. T. Garvey<sup>m</sup> V. Genty<sup>g</sup>  
D. Goeldi<sup>a</sup> S. Gollapinni<sup>z</sup> E. Gramellini<sup>ee</sup> H. Greenlee<sup>h</sup> R. Grosso<sup>e</sup> R. Guenette<sup>s,i</sup>  
P. Guzowski<sup>n</sup> A. Hackenburg<sup>ee</sup> P. Hamilton<sup>x</sup> O. Hen<sup>o</sup> J. Hewes<sup>n</sup> C. Hill<sup>n</sup> J. Ho<sup>d</sup>  
G. A. Horton-Smith<sup>k</sup> A. Hourlier<sup>o</sup> E.-C. Huang<sup>m</sup> C. James<sup>h</sup> J. Jan de Vries<sup>c</sup> L. Jiang<sup>u</sup>  
R. A. Johnson<sup>e</sup> J. Joshi<sup>b</sup> H. Jostlein<sup>h</sup> Y.-J. Jwa<sup>g</sup> D. Kaleko<sup>g</sup> G. Karagiorgis<sup>g</sup> W. Ketchum<sup>h</sup>  
B. Kirby<sup>b</sup> M. Kirby<sup>h</sup> T. Kobilarcik<sup>h</sup> I. Kreslo<sup>a</sup> Y. Li<sup>b</sup> A. Lister<sup>l</sup> B. R. Littlejohn<sup>j</sup> S. Lockwitz<sup>h</sup>  
D. Lorca<sup>a</sup> W. C. Louis<sup>m</sup> M. Luethi<sup>a</sup> B. Lundberg<sup>h</sup> X. Luo<sup>ee</sup> A. Marchionni<sup>h</sup> S. Marocci<sup>h</sup>  
C. Mariani<sup>dd</sup> J. Marshall<sup>c</sup> D. A. Martinez Caicedo<sup>j</sup> A. Mastbaum<sup>d</sup> V. Meddage<sup>k</sup> T. Miceli<sup>q</sup>  
G. B. Mills<sup>m</sup> A. Mogan<sup>z</sup> J. Moon<sup>o</sup> M. Mooney<sup>b,f</sup> C. D. Moore<sup>h</sup> J. Mousseau<sup>p</sup> M. Murphy<sup>dd</sup>  
R. Murrells<sup>n</sup> D. Naples<sup>u</sup> P. Nienaber<sup>y</sup> J. Nowak<sup>l</sup> O. Palamara<sup>h</sup> V. Pandey<sup>dd</sup> V. Paolone<sup>u</sup>  
A. Papadopoulou<sup>o</sup> V. Papavassiliou<sup>q</sup> S. F. Pate<sup>q</sup> Z. Pavlovic<sup>h</sup> E. Piasetzky<sup>y</sup> D. Porzio<sup>n</sup>  
G. Pulliam<sup>x</sup> X. Qian<sup>b</sup> J. L. Raaf<sup>h</sup> V. Radeka<sup>b</sup> A. Rafique<sup>k</sup> L. Rochester<sup>w</sup> M. Ross-Lonergan<sup>g</sup>  
C. Rudolf von Rohr<sup>a</sup> B. Russell<sup>ee</sup> D. W. Schmitz<sup>d</sup> A. Schukraft<sup>h</sup> W. Seligman<sup>g</sup>  
M. H. Shaevitz<sup>g</sup> J. Sinclair<sup>a</sup> A. Smith<sup>c</sup> E. L. Snider<sup>h</sup> M. Soderberg<sup>x</sup> S. Söldner-Rembold<sup>n</sup>  
S. R. Soleti<sup>s,i</sup> P. Spentzouris<sup>h</sup> J. Spitz<sup>p</sup> J. St. John<sup>e,h</sup> T. Strauss<sup>h</sup> K. Sutton<sup>g</sup>  
S. Sword-Fehlberg<sup>q</sup> A. M. Szeln<sup>n</sup> N. Tagg<sup>r</sup> W. Tang<sup>z</sup> K. Terao<sup>g,w</sup> M. Thomson<sup>c</sup> C. Thorn<sup>b</sup>  
M. Touns<sup>h</sup> Y.-T. Tsai<sup>w</sup> S. Tufanli<sup>ee</sup> T. Usher<sup>w</sup> W. Van De Pontseele<sup>s,i</sup> R. G. Van de Water<sup>m</sup>  
B. Viren<sup>b</sup> M. Weber<sup>a</sup> H. Wei<sup>b</sup> D. A. Wickremasinghe<sup>u</sup> K. Wierman<sup>t</sup> Z. Williams<sup>aa</sup> S. Wolbers<sup>h</sup>  
T. Wongjirad<sup>o,cc</sup> K. Woodruff<sup>q</sup> T. Yang<sup>h</sup> G. Yarbrough<sup>z</sup> L. E. Yates<sup>o</sup> B. Yu<sup>b</sup> G. P. Zeller<sup>h</sup>  
J. Zennaro<sup>d</sup> C. Zhang<sup>b</sup>

<sup>a</sup>Universität Bern, Bern CH-3012, Switzerland

<sup>b</sup>Brookhaven National Laboratory (BNL), Upton, NY, 11973, USA

<sup>c</sup>University of Cambridge, Cambridge CB3 0HE, United Kingdom

<sup>d</sup>University of Chicago, Chicago, IL, 60637, USA

<sup>e</sup>University of Cincinnati, Cincinnati, OH, 45221, USA  
<sup>f</sup>Colorado State University, Fort Collins, CO, 80523, USA  
<sup>g</sup>Columbia University, New York, NY, 10027, USA  
<sup>h</sup>Fermi National Accelerator Laboratory (FNAL), Batavia, IL 60510, USA  
<sup>i</sup>Harvard University, Cambridge, MA 02138, USA  
<sup>j</sup>Illinois Institute of Technology (IIT), Chicago, IL 60616, USA  
<sup>k</sup>Kansas State University (KSU), Manhattan, KS, 66506, USA  
<sup>l</sup>Lancaster University, Lancaster LA1 4YW, United Kingdom  
<sup>m</sup>Los Alamos National Laboratory (LANL), Los Alamos, NM, 87545, USA  
<sup>n</sup>The University of Manchester, Manchester M13 9PL, United Kingdom  
<sup>o</sup>Massachusetts Institute of Technology (MIT), Cambridge, MA, 02139, USA  
<sup>p</sup>University of Michigan, Ann Arbor, MI, 48109, USA  
<sup>q</sup>New Mexico State University (NMSU), Las Cruces, NM, 88003, USA  
<sup>r</sup>Otterbein University, Westerville, OH, 43081, USA  
<sup>s</sup>University of Oxford, Oxford OX1 3RH, United Kingdom  
<sup>t</sup>Pacific Northwest National Laboratory (PNNL), Richland, WA, 99352, USA  
<sup>u</sup>University of Pittsburgh, Pittsburgh, PA, 15260, USA  
<sup>v</sup>Saint Mary's University of Minnesota, Winona, MN, 55987, USA  
<sup>w</sup>SLAC National Accelerator Laboratory, Menlo Park, CA, 94025, USA  
<sup>x</sup>Syracuse University, Syracuse, NY, 13244, USA  
<sup>y</sup>Tel Aviv University, Tel Aviv, Israel, 69978  
<sup>z</sup>University of Tennessee, Knoxville, TN, 37996, USA  
<sup>aa</sup>University of Texas, Arlington, TX, 76019, USA  
<sup>bb</sup>TUBITAK Space Technologies Research Institute, METU Campus, TR-06800, Ankara, Turkey  
<sup>cc</sup>Tufts University, Medford, MA, 02155, USA  
<sup>dd</sup>Center for Neutrino Physics, Virginia Tech, Blacksburg, VA, 24061, USA  
<sup>ee</sup>Yale University, New Haven, CT, 06520, USA

E-mail: [microboone\\_info@fnal.gov](mailto:microboone_info@fnal.gov)

**ABSTRACT:** We describe the concept and procedure of drifted-charge extraction developed in the MicroBooNE experiment, a single-phase liquid argon time projection chamber (LArTPC). This technique converts the raw digitized TPC waveform to the number of ionization electrons passing through a wire plane at a given time. A robust recovery of the number of ionization electrons from both induction and collection anode wire planes will augment the 3D reconstruction, and is particularly important for tomographic reconstruction algorithms. A number of building blocks of the overall procedure are described. The performance of the signal processing is quantitatively evaluated by comparing extracted charge with the true charge through a detailed TPC detector simulation taking into account position-dependent induced current inside a single wire region and across multiple wires. Some areas for further improvement of the performance of the charge extraction procedure are also discussed.

**KEYWORDS:** MicroBooNE, Signal Processing, Deconvolution, ROI

---

## Contents

<b>1</b>	<b>Introduction</b>	<b>2</b>
<b>2</b>	<b>LArTPC signal formation</b>	<b>4</b>
2.1	Field response	4
2.2	Electronics response	11
2.3	Topology-dependent TPC signals	12
<b>3</b>	<b>Reconstruction of drifted electron distribution</b>	<b>15</b>
3.1	Signal extraction principles	15
3.1.1	Deconvolution and software filters	18
3.1.2	2D deconvolution	19
3.1.3	Region of interest (ROI)	20
3.2	Method	22
3.2.1	Position-averaged response functions	23
3.2.2	Software filters	24
3.2.3	Identification of signal ROIs	26
3.2.4	Refinement of ROIs	29
<b>4</b>	<b>Evaluating TPC signal processing with simulation</b>	<b>31</b>
4.1	Key simulation improvements	32
4.2	Simulation overview	33
4.2.1	Initial distribution of charge depositions	35
4.2.2	Drift transport and physics	35
4.2.3	Detector field and electronics response	36
4.2.4	Performing the convolution	37
4.2.5	Truth values	39
4.2.6	Noise simulation	39
4.3	Quantitative evaluation of the signal processing	41
4.3.1	Basic performance of the signal processing	42
4.3.2	Charge resolution due to electronics noise	44
4.3.3	Charge bias due to thresholding in ROI finding	46
4.3.4	Inefficiency of line charge extraction	46
4.3.5	Performance of line charge extraction	46
<b>5</b>	<b>Discussion</b>	<b>50</b>
5.1	Limitations of 2D field responses	50
5.2	Limitations of the current ROI finding	52
5.3	Impact of excess noise in real data	54

## 1 Introduction

The liquid argon time projection chamber (LArTPC) [1–4] is an innovative detector technology being actively developed worldwide. Several features of the LArTPC make it well adapted to the study of neutrinos and other rare processes. Argon is readily available commercially ( $\sim 1\%$  by volume, the most abundant noble gas in the atmosphere). Free electrons have high mobility, low diffusion [5], and very high survival time in pure liquid argon (LAr), making it an attractive material for a TPC. In addition, LAr has a relatively high density and a high scintillation light yield. In the near term, the Short-Baseline Neutrino Program [6] will utilize three LArTPCs (MicroBooNE, SBND, and ICARUS) at Fermi National Accelerator Laboratory (Fermilab) to search for eV-scale sterile neutrino(s) and measure neutrino-argon interaction cross sections. In the long term, the long-baseline Deep Underground Neutrino Experiment (DUNE) [7] is planning to use four large 10 kilotons LArTPC modules as far detectors to search for leptonic CP violation, determine the neutrino mass hierarchy, test the standard three-neutrino paradigm, search for proton decays, and potentially observe supernova neutrino bursts. The development of high-quality and fully-automated event reconstruction algorithms for LArTPC neutrino detectors is crucial to the success of the short-baseline and long-baseline physics programs and is an area of significant activity [8–11]. The robust recovery of the ionization signals from the LArTPC images is the critical first stage of LArTPC reconstruction.

The MicroBooNE detector [12] is the first LArTPC in the Short-Baseline Neutrino Program [6] to be operational. It is a single-phase LArTPC built to observe interactions of neutrinos from the on-axis Booster [13] and off-axis NuMI [14] beams at Fermi National Accelerator Laboratory in Batavia, IL. The TPC LAr volume is  $2.56\text{ m} \times 2.3\text{ m} \times 10.4\text{ m}$  with about 90 metric tons active mass, housed in a foam-insulated evacuable cryostat vessel. At the anode end of the 2.56 m drift distance, there are three parallel wire readout planes [15]. The first wire plane facing the cathode is labeled "U", and the second and third plane are labeled "V" and "Y", respectively. The wire pitch and the gap between two adjacent wire planes are both 3 mm. The 3456 wires in the Y plane are oriented vertically. The U and V planes each contain 2400 wires oriented  $\pm 60^\circ$  with respect to vertical. Behind the wire planes and external to the TPC, there is an array of 32 photomultiplier tubes [16] to detect scintillation light for triggering, timing, and other purposes.

The TPC signal formation in MicroBooNE is illustrated in figure 1. At a drift field of  $273\text{ V/cm}$  corresponding to a cathode high voltage of  $-70\text{ kV}$ , the ionization electrons drift through the LAr detector volume along the electric field lines at a nominal speed of about  $1.10\text{ mm}/\mu\text{s}$  toward the anode wire planes. Different bias voltages,  $-110\text{ V}$ ,  $0\text{ V}$ , and  $230\text{ V}$  are applied to the U, V, and Y wire planes, respectively, to ensure all ionization electrons pass through the U and V planes before being collected by the Y plane [17] at the nominal MicroBooNE operating voltage of  $-70\text{ kV}$ . As ionization electrons drift towards and then past the wires of the U and V planes, currents with bipolar shape are induced on the U and V planes. In contrast, a unipolar-shaped current is induced

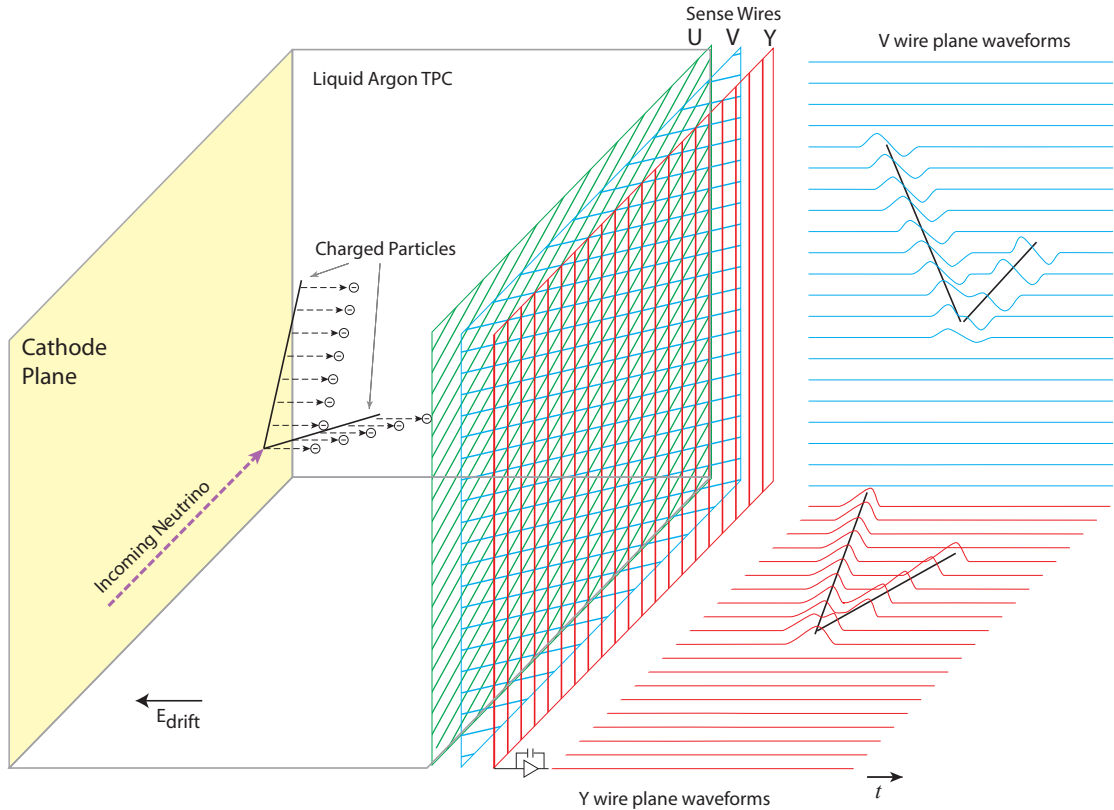


**Figure 1:** Diagram illustrating the signal formation in a LArTPC with three wire planes [12]. The signal on each plane produces a 2D image of the event. For simplicity, the signal in the U induction plane is omitted from the diagram.

on a wire of the Y plane as all nearby ionization charge is collected. The U and V wire planes are commonly referred to as the induction planes. Although also measuring induced current, the Y wire plane is commonly referred to as the collection plane.

While the collection plane signal is mostly unipolar and large in amplitude with a Gaussian time profile, the induction plane signal is bipolar and small in amplitude with a complex time profile. The latter is due to the overlapping of many bipolar signal shapes as a distribution of drifting charge passes near the wires. Despite complications in the induction plane signal, the combination of the induction and collection wire planes is essential for tomographic event reconstruction [11] in single-phase LArTPCs. Leveraging the induction signal in combination with the collection signal is important to fully exploit single-phase LArTPC capabilities.

The implementation of the induction and collection wire readout planes is a unique feature of the current single-phase LArTPC detectors. An alternative readout scheme, 2D pixel readout, would not suffer from ailments introduced from the complexity of the induction plane signal. However,

this alternative scheme for large detectors is not actionable at present, though good progress has been made [18]. If the wire readout in MicroBooNE were replaced by a full 2D pixel readout, the total number of channels would be 2.7 million instead of 8,256, resulting in a significant increase in the cost of electronics. Furthermore, the power consumption of these electronics inside LAr would be a serious concern. Given the wire readout technology employed in the single-phase LArTPCs, reconstruction of the charge passing through the induction wire plane improves the correlation of signal between the multiple anode plane views and helps resolve degeneracies inherent in a projective wire geometry.

The successful reconstruction of a 3D event topology generally requires robust signal extraction in multiple 2D projection views. Since the ionization electrons are not collected on any of the induction wire planes, they naturally provide additional non-destructive views of the ionization electrons from the charged particle tracks. A successful extraction of the ionization electron information from the complicated induction plane signals is essential for 3D event reconstruction in single-phase LArTPCs using tomographic reconstruction and is expected to further enhance 3D reconstruction for techniques that match the image in different 2D projection views.

This paper is organized as follows. In section 2, we review the process of TPC signal formation including the induced current generation, signal amplification and shaping, as well as the impact of noise. In section 3, we describe the principle and the algorithm implemented to extract ionization charge from the TPC signal. The performance of the TPC signal processing chain is then evaluated with a detailed TPC simulation in section 4. The assessment of this signal processing technique on MicroBooNE data is provided in a dedicated accompanying paper [19]. A discussion of some identified limitations of the current techniques is in section 5. A summary and prospects for future improvements are presented in section 6.

## 2 LArTPC signal formation

The formation of the TPC signal consists of three parts: i) the electric field response to the drifting of a point ionization charge leading to induced currents on the sense wires, ii) the electronics response to the induced current waveform input to each channel in terms of amplification and shaping, and iii) the initial distribution of the ionization charge in the bulk of the detector, how this charge drifts in the applied electric field and how it undergoes diffusion and absorption as it drifts. In the following sections, we describe each part in detail.

### 2.1 Field response

When ionization electrons drift past the initial two induction wire planes toward the final collection wire plane, current is induced on nearby wires. Henceforth, we refer to the induced current on one wire due to a single electron charge as a field response function. The principle of current induction is described by Ramo's theorem [20]. An element of ionization charge  $q$  in motion at a given location induces a current  $i$  on some electrode (wire),

$$i = -q\vec{E}_w \cdot \vec{v}_q. \quad (2.1)$$

This current is proportional to the inner product of a constructed weighting field  $\vec{E}_w$  for a given wire and the drift velocity  $\vec{v}_q$  of the charge at the given location. The weighting field  $\vec{E}_w$  only

depends on the geometry of the electrodes and can be calculated by removing the drifting charge, placing the targeted electrode at unity potential, and setting all other conductors to ground. For a single medium, the weighting potential is independent of the dielectric properties/constants. For multiple media, the weighting potential must be calculated taking into account each material's dielectric properties. This result is valid in the quasi-static approximation and in arbitrary linear media where the permittivity is independent of the potentials [21, 22]. A generalized form of the weighting potential considering non-linear effects can also be found in [21] and [22]. The charge's drifting velocity  $\vec{v}_q$  is a function of the external electric field, which depends on the geometry of the electrodes as well as the applied drifting and bias voltages and liquid argon temperature. Figure 2 shows electron drift paths in an applied electric field as well as lines of equal potentials for the weighting field for the U, V, and Y wire planes in MicroBooNE. The electron drift paths and the weighting fields are calculated using the Garfield [23] software. These calculations adopt a 2D model of a portion of MicroBooNE near a subset of wires. Some limitations in this model are discussed in section 5.1.

Although equation 2.1 fully describes a field response function for a given point charge at a given moment in time, the easiest way to understand the qualitative behavior of the field response function is through the integral of the induced current and its connection to Green's reciprocity theorem. Let's consider a case where a point charge  $q_m$  is moving in an inter-electrode space. If we then assume that the charge  $q_m$  is on an infinitesimal electrode and the sensing electrode is labeled as electrode I, then by Green's reciprocity,

$$q_m \cdot V_m = Q_I \cdot V_I. \quad (2.2)$$

Here  $Q_I$  is the charge on the sensing electrode induced by  $q_m$ .  $V_m$  is the potential at the location of  $q_m$  introduced by the sensing electrode potential  $V_I$ . With equation 2.2, we can derive the induced current as

$$i = \frac{dQ_I}{dt} = q_m \cdot \vec{\nabla} V_w \cdot \frac{d\vec{r}}{dt}, \quad (2.3)$$

where the weighting potential<sup>1</sup> is a dimensionless quantity defined as  $V_w = V_m/V_I$ . It is easy to see that the above equation recovers equation 2.1 where  $\vec{\nabla} V_w$  corresponds to  $-\vec{E}_w$  and  $\frac{d\vec{r}}{dt}$  is the velocity of the charge  $q_m$ . Given equation 2.3, the integral of the induced current due to a charge  $q_m$  moving along its drift path

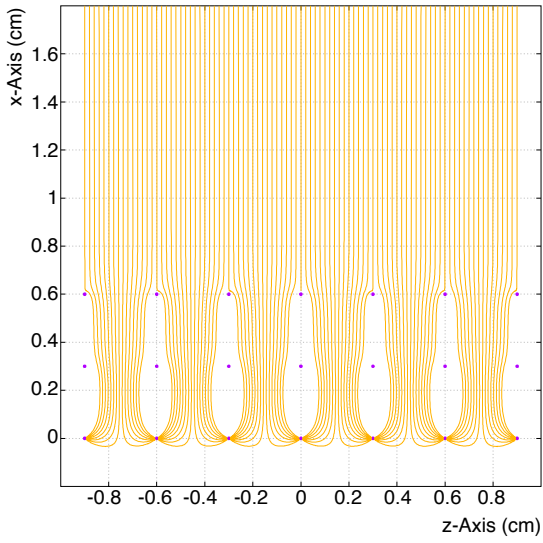
$$\int i dt = q_m \cdot (V_w^{end} - V_w^{start}) \quad (2.4)$$

is proportional to the difference of the weighting potential at the end and start of the path.

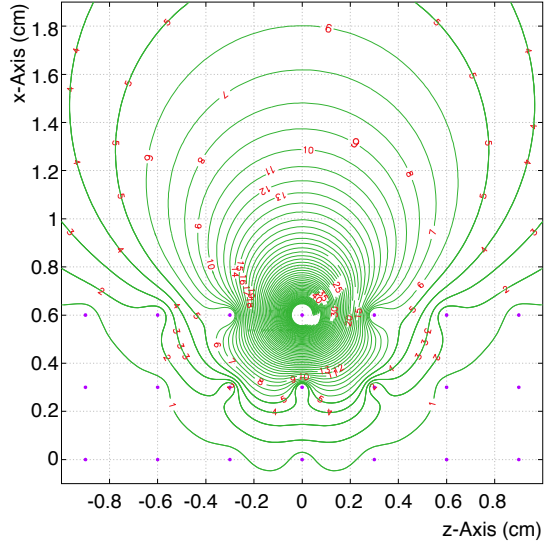
For signal processing and signal simulation, the field response functions for a single ionization electron traveling over a number of possible discrete drift paths are calculated with the Garfield program [23] using a 2D model for MicroBooNE wires with a scheme illustrated in figure 3. The calculation utilizes a region that spans 22.4 cm (the upper boundary at 20.4 cm in front of the Y plane) along the nominal electron drift direction and 30 cm perpendicular to both the drift direction and the wire orientation. In the calculation, each wire plane contains 101 wires with 150  $\mu\text{m}$  diameter separated by a 3 mm wire pitch. The drifting field (273 V/cm) is achieved by setting the

---

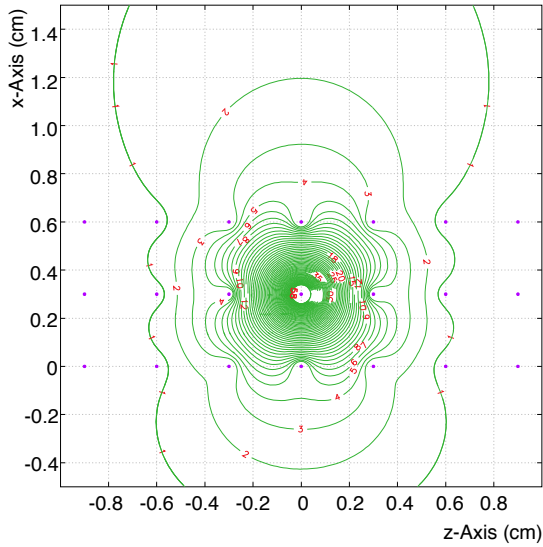
<sup>1</sup>This is equivalent to the definition from Ramo's theorem, where the voltage on the electrode under consideration is set to 1 V and all others are set to 0 V.



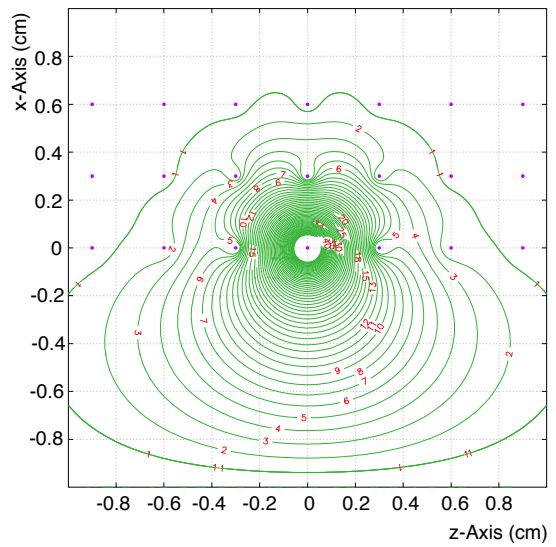
(a) Electron drift paths.



(b) Weighting potential on a U wire.



(c) Weighting potential on a V wire.



(d) Weighting potential on a Y wire.

**Figure 2:** A demonstration of electron drift paths in the applied electric field (panel a) and weighting potentials (panels b, c, d) on individual wires of the 2D MicroBooNE TPC model, using the Garfield program. The coordinates for each plane are defined in section 2.3 as shown in figure 8a. The x-Axis is in the drifting field direction and the z-Axis is in the beam direction. The weighting potential is a dimensionless quantity, given as a value relative to the to the electric potential on the target wire. Values for the weighting potential are indicated in percentage on each equipotential line, ranging from 1% for the farthest to 60% for the closest illustrated.



negative voltage at the upper boundary of the simulated area. The nominal MicroBooNE operating bias voltages for each wire plane are used in the calculation.

There are two stages in calculating the field response functions. The first one is the calculation of the electron drift paths in the applied electric field as shown in figure 2a. The second stage is the calculation of the weighting electric potentials as shown in the remaining panels of figure 2. The induced current can be calculated following equation (2.1). The electron drift velocity as a function of electric field is taken from recent measurements [5, 24]. For these single-electron simulations, diffusion is omitted.

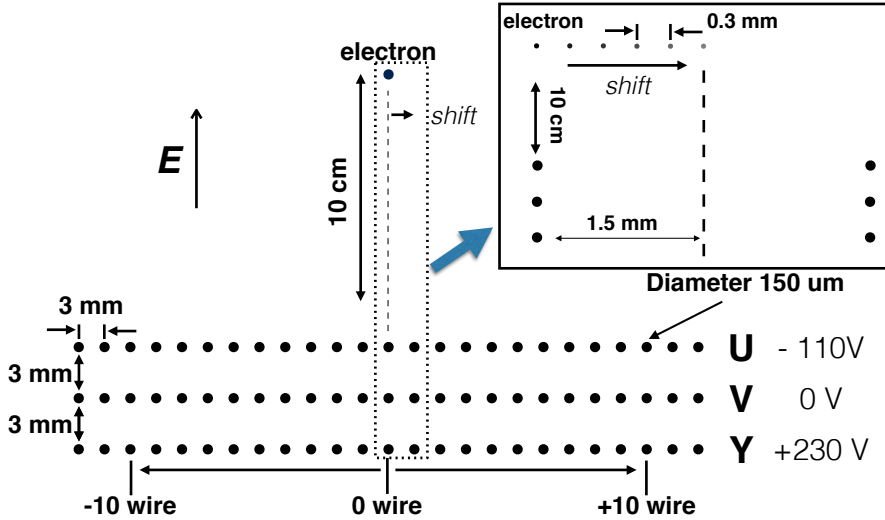


**Figure 3:** Illustration of the 2D Garfield simulation scheme (dimensions not to scale), where black dots indicate individual wires. MicroBooNE’s anode plane-to-plane spacing is 3 mm, with 3 mm wire pitch in each plane. The inset denotes the sub-pitch designation of electron drift paths whereupon the field response is calculated.

For a single drift path calculation, the electron starts from a point 10 cm away from the wire plane above the central wire (shown as “0 wire” in figure 3). The field response functions for that central wire and  $\pm 10$  wires on both sides (21 wires in total) are calculated. The simulation is then repeated starting at different transverse locations, each shifted by 0.3 mm from the previous, spanning 0 mm to 1.5 mm. In total, 126 field responses (six electron positions  $\times$  21 readout wires) are calculated. In the described 2D scheme, the inter-plane wires are aligned. The shift in relative inter-plane 2D geometry is a 3D effect and has minimal impact on the calculated field response shape.

Figure 4 shows the overall response functions for each wire of interest for induction U (top panel), induction V (middle panel), and collection Y (bottom panel) wire planes, where the overall response is the field responses convolved with the electronics response (to be described in section 2.2). The X-axis in figure 4 is the initial transverse position of the ionization electron relative to the central wire of each plane and expressed in units of wire number. Each wire region ( $\pm 0.5$  wire pitch) is sampled by 11 electron drift paths with starting points that are regularly separated by 0.3 mm. The field response on the central wire for a single path is thus represented by a slice

of this plot at a corresponding location on the X-axis for the given path. The Y-axis is the drift time relative to the electron arriving at the V plane. Time is made discrete in units of  $0.5 \mu\text{s}$  (one “tick”) which corresponds to the analog-to-digital converter (ADC) sampling period employed by the MicroBooNE readout electronics.

The normalization of the overall response function is chosen so that the integral of the response function of the closest wire from the collection Y plane is unity, which corresponds to a single electron. To emphasize the shape of the field response functions, a special scale labeling with “Log10” is used to set the color scale of the induced current  $i$  (electrons per  $0.5 \mu\text{s}$ ) in Figure 4:

$$i \text{ in “Log 10”} = \begin{cases} \log_{10}(i \cdot 10^5), & \text{if } i > 1 \times 10^{-5}, \\ 0, & \text{if } -1 \times 10^{-5} \leq i \leq 1 \times 10^{-5}, \\ -\log_{10}(-1 \cdot i \cdot 10^5) & \text{if } i < -1 \times 10^{-5}. \end{cases} \quad (2.5)$$

The 2D nature of the model used for MicroBooNE wire planes in the Garfield calculation described above is an approximation of the actual detector. No detector edge effects are considered and the 2D nature of the model implies that wires are effectively infinite in length and that any effects due to the wires crossing near each other can not be included. An initial set of field calculations has been performed with custom software that utilizes a 3D model of the MicroBooNE wire planes. More discussions can be found in section 5.1.

Given the results shown above, we can conclude the following:

- As an ionization electron moves towards the closest induction plane wire, it climbs up the corresponding induction wire weighting potential; therefore, the induced current is negative and corresponds to the positive voltage waveform shown in this paper following the MicroBooNE electronics readout convention.
- As an ionization electron passes the induction wire plane and moves toward the collection wire plane, the induction wire weighting potential decreases and the induced current changes sign. This results in the bipolar shape for the induction plane signals. See examples in figure 5.
- As an ionization electron drifts towards the wire on which it will eventually be collected (the central wire), the weighting function for that wire always increases. Consequently, collection wire signals are unipolar in shape.
- For an ionization electron originating from the cathode plane (i.e. weighting potential zero), the integrated induction charge in an induction wire plane is nominally zero, since the electron ultimately ends up at a collection wire for which the corresponding induction wire weighting potential is also zero. Similarly, the integrated induction charge in the collection wire should be equal to the charge of one electron, as the corresponding collection wire weighting potential is unity.
- The above conclusion about the integrated induction charge is no longer true for an ionization electron generated inside the active LArTPC volume due to a non-zero weighting potential at the point of origin. The deviation from zero integrated charge is largest for the first induction

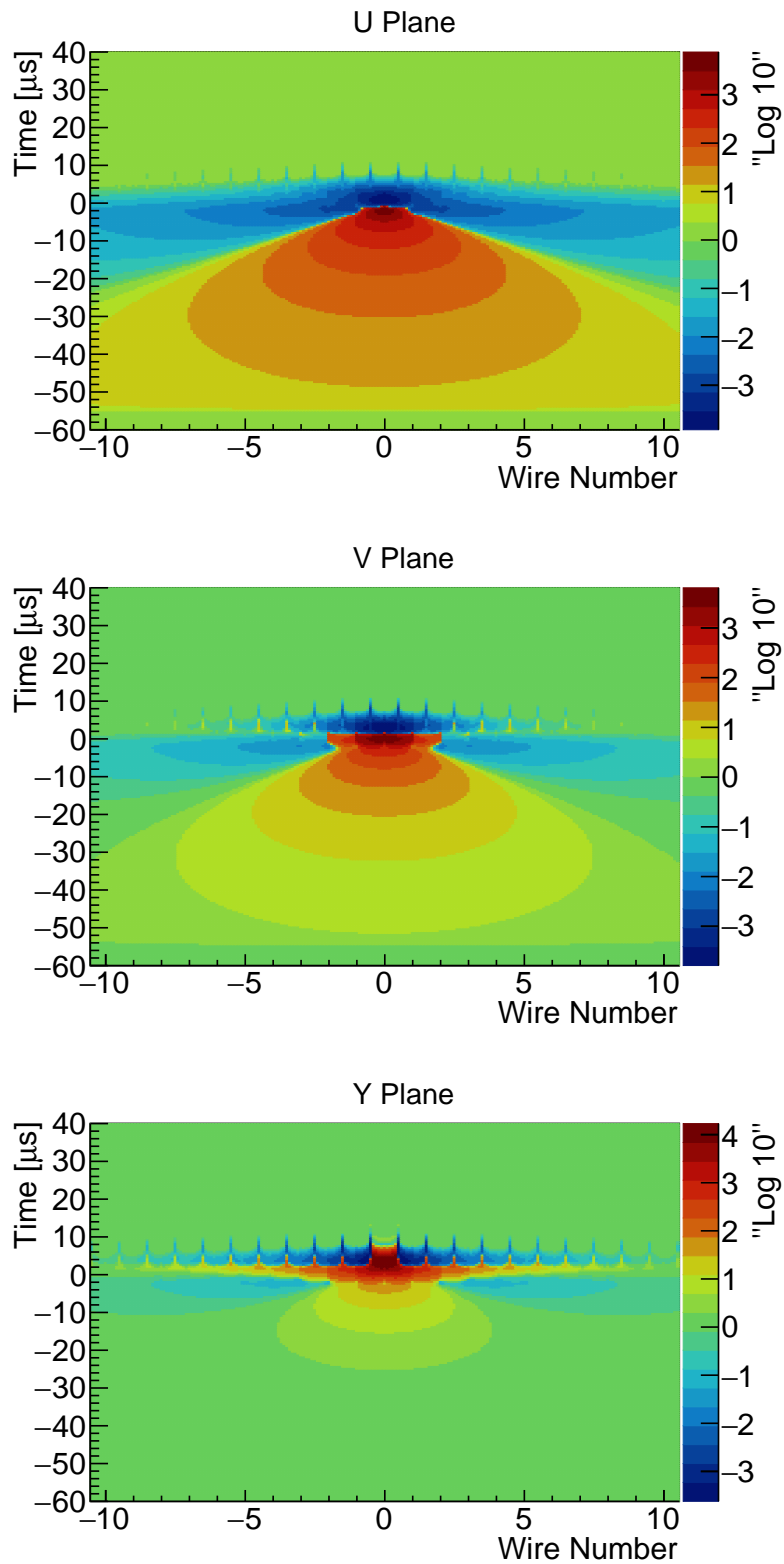


**Figure 4:** The overall response functions after convolving the field response function and an electronics response function with a  $2\ \mu\text{s}$  peaking time are shown in two dimensions. All plots are shown in “Log10” scale.

U plane, as V and Y wire planes are shielded by the U plane thus their weighting fields do not extend as far into the volume. However, even for the most extreme case, these deviations are generally limited to a few percent for points of origin 10 cm away from the U wire plane. We should also note that the induced current due to the sudden creation of the ionization electron is balanced by the creation of the positive argon ion.<sup>2</sup>

- The strength of the induced current on an induction plane wire due to an ionization electron is related to the maximum weighting potential that the electron can reach. Therefore, we expect the induction signal to increase as a given electron is allowed to pass closer to the wire. However, the bias voltage applied to each wire plane forces the electrons to divert from regions of maximum induction wire weighting potential. This causes the induction signals to be generally smaller than those on collection wires.
- Since the weighting field of the sense wire extends far beyond the sense wire region, an ionization electron drifting far away from a sense wire will still prompt induced current on the sense wire, although at a reduced strength. Therefore, the induced current depends on the local charge density, which is further determined by the event topology.
- The time duration of the induced current (field response) depends on the drift velocity of the ionization electron as well as the electrode geometry. For the U wire plane, the induced current becomes sizable when the ionization electron is about several cm away from the wire plane and ends when the electron is collected by the Y wire plane. For the V wire plane, the induced current becomes sizable when the electron is about to pass the U wire plane and also ends when the electron is collected by the Y wire plane. For the Y plane, the induced current becomes sizable as the electron is about to pass the U wire plane. These field response functions are further modified for a cloud of electrons due to different drift paths. In particular, broadening is expected for the collection wire response function for a cloud of electrons.
- As illustrated in figure 2a, there exist variations in the drift paths of ionization electrons toward the collection wire. This results in fine structures (see figure 5) in the field response which are dependent on the drifting path as well as the weighting potential shown in figure 2. In particular, an electron traveling along a path equidistant from two collection wires (at the boundary of one wire pitch) will be collected with a few  $\mu\text{s}$  delay compared to one that arrives at its collection wire more directly. The phase space for this delay is small so it affects a minority of drifting charge. Integrated over a distribution of ionization electrons, this variation contributes to a broadening of the overall collection signal as shown in the bottom panel of figure 7. The second negative peak in the field response of the induction wire as shown in figure 5 originates from (and thus coincides with) the collection of the ionization electron in the collection wire. However, due to shielding from the V plane (see weighting potential in figure 2), this peak for the U plane is insignificant.

---

<sup>2</sup>At creation,  $\int idt = \sum_m q_m \cdot v_w^{end} = 0$ , since  $\sum_m q_m = 0$ . However, immediately following creation, the ion drift velocity is  $O(10^6)$  smaller than the electron drift velocity. Thus, drift of the  $\text{Ar}^+$  contributes negligibly to the induced current.

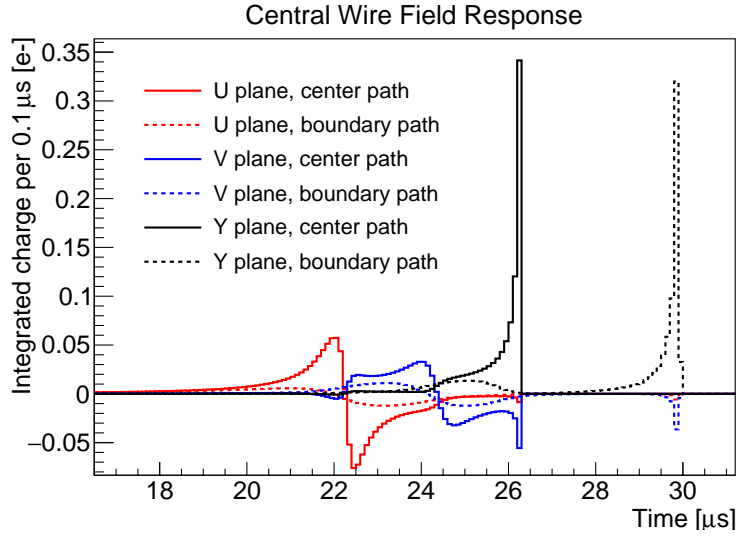


**Figure 5:** Field responses (induced-current) from various paths of one drifting ionization electron for the three wire planes. Y-axis is the integrated charge over  $0.1 \mu\text{s}$ . Within the central wire pitch, a center path at  $0 \text{ mm}$  (solid) and a boundary path at  $1.5 \text{ mm}$  (dashed) are employed for this demonstration. See figure 3 for an illustration of the simulated geometry. The fine structures in the field responses are subject to the path of the drifting ionization electron and the weighting potential as shown in figure 2.

## 2.2 Electronics response

The induced current on the wire is received, amplified, and shaped by a pre-amplifier. This process is described by the electronics response function. The impulse response function in the time domain is shown in figure 6a. The MicroBooNE front-end cold electronics [25] are designed to be programmable with four different gain settings ( $4.7 \text{ mV/fC}$ ,  $7.8 \text{ mV/fC}$ ,  $14 \text{ mV/fC}$  and  $25 \text{ mV/fC}$ ) and four peaking time settings ( $0.5 \mu\text{s}$ ,  $1.0 \mu\text{s}$ ,  $2.0 \mu\text{s}$  and  $3.0 \mu\text{s}$ ). In MicroBooNE, the gain is roughly  $3.5\%$  lower than expected and the peaking time is  $10\%$  higher than expected [19]. For a fixed gain setting, the peak of the impulse response is always at the same height independent of the peaking time. The peaking time is defined as the time difference between  $5\%$  of the peak at the rising edge and the peak. The different gain settings allow for applications with differing ranges of input signal strength. The four peaking time settings are provided to satisfy the Nyquist criterion [26] at different sampling rates. Two additional RC filters are exploited to remove the baseline from the pre-amplifier and the intermediate amplifier. The intermediate amplifier provides an additional gain of  $1.2$  (dimensionless) to compensate for the loss without any shaping/filtering. The time-domain impulse response is as follows (and is shown in figure 6b):

$$\text{Single RC} : h(t) = \delta(t) - \frac{1}{\tau} \cdot e^{-t/\tau} u(t), \quad (2.6)$$

$$\text{RC} \otimes \text{RC} : h(t) = \delta(t) + \left(\frac{t}{\tau} - 2\right) \frac{1}{\tau} \cdot e^{-t/\tau} u(t), \quad (2.7)$$

where the time constant  $\tau = RC$  and  $\delta(t)$ ,  $u(t)$  are the delta function and the step function, respectively. In general, the time constant is  $1 \text{ ms}$  in MicroBooNE and the RC filter effect is visible when

the signal is large or long enough.

The resulting signal waveform, as illustrated in figure 7, after electronics shaping is then digitally sampled at 2 MHz by a 12-bit ADC with the input voltage ranging from 0 to 2 V. More details regarding the performance of MicroBooNE cold electronics can be found in [27].

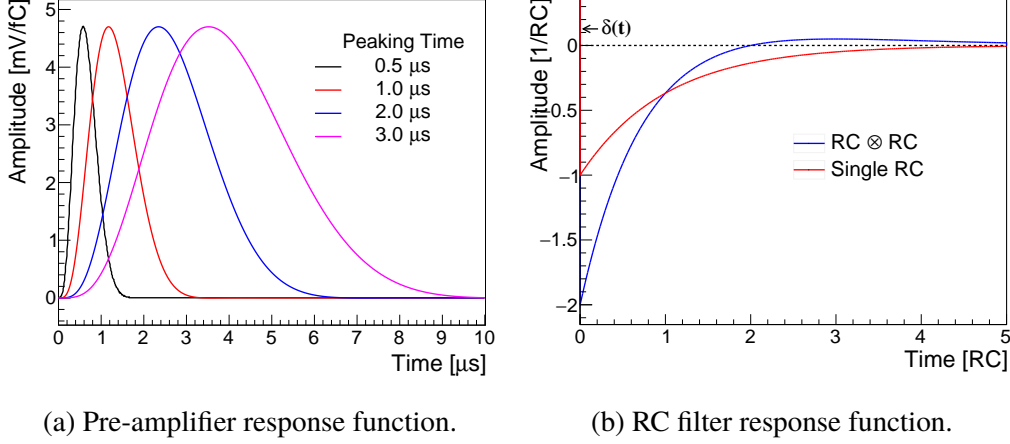


**Figure 6:** MicroBooNE pre-amplifier electronics impulse response functions are shown for (a) four peaking time settings at 4.7 mV/fC gain and (b) a single RC filter and two independent RC filters ( $RC \otimes RC$ ).

### 2.3 Topology-dependent TPC signals

As shown in figure 2, the weighting potential is not confined to just the region around one sense wire. An element of drifting ionization charge will induce signal on many wires in its vicinity. The signal of any one wire depends on the ensemble distribution of charge in its neighborhood. To illustrate this effect, we first consider the signal resulting from an isochronous (parallel to the anode plane) minimum ionizing particle (MIP) track perpendicular to each anode plane wire orientation. Figure 7 shows the simulated central wire signal when the contributions of ionization charge at different positions beyond the central wire are considered. For all three wire planes, the signal contribution due to long-range induced current for ionization charge is non-negligible. For the induction V and collection Y wire planes, the proportion of the wire signal is small for ionization charge beyond a couple wires from the central wire. For the induction U wire plane, which is the first wire plane facing the active TPC region, the contribution of the wire signal from distant wires can be sizable for the ionization charge as far as 10 wires away from the central wire. The modification of the signal due to this long range induction effect is relatively small for the collection wires, since the two induction planes provide shielding. The unipolar induction signal from any collected electrons on the collection plane is large compared to the bipolar contributions from electrons which collect on neighboring wires. On the other hand, signal distortion due to long range induction can be sizable for the induction wires due to their smaller field response functions and the potential cancellation of multiple bipolar signals. This is also true for adjacent collection plane wires which did not actually collect the ionization charge. They effectively behave as induction wires.

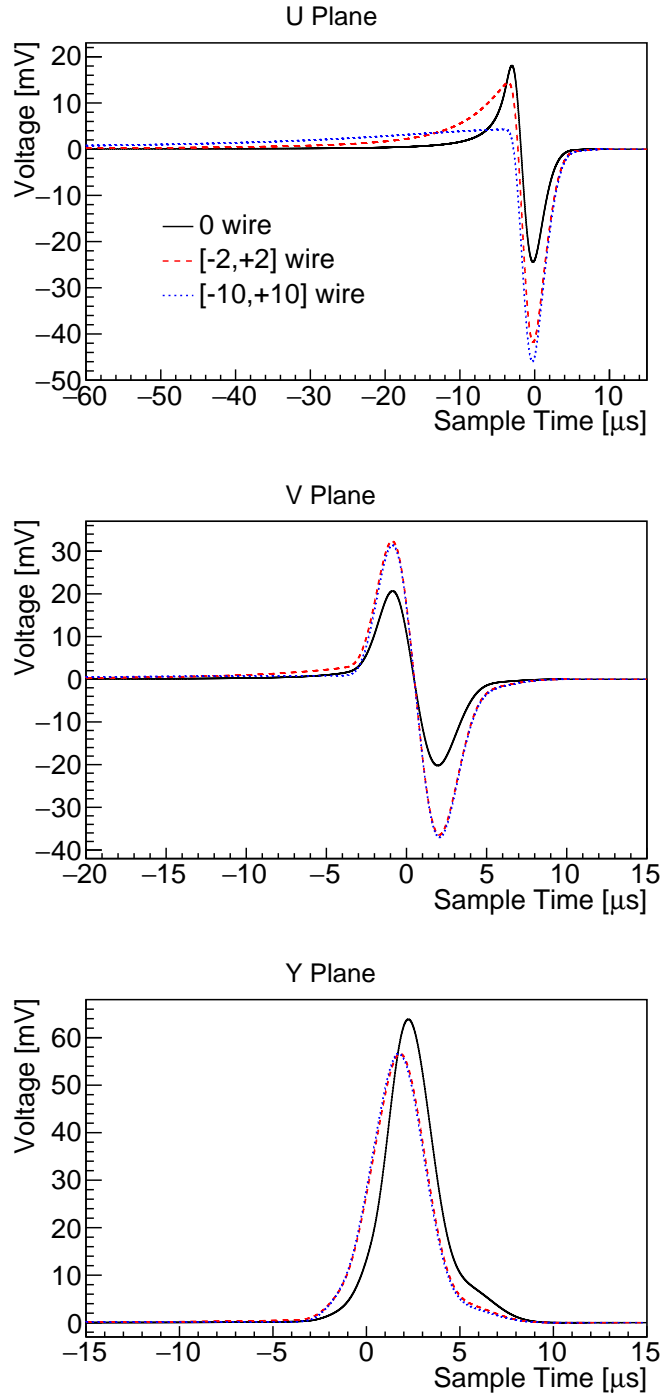


**Figure 7:** Simulated baseline-subtracted TPC signals for an ideal isochronous MIP track traveling perpendicular to each wire plane orientation ( $\theta_{xz} = 0^\circ$  and  $\theta_y = 90^\circ$ , i.e. along the  $z$ -axis, wire pitch direction, for each wire plane) for MicroBooNE wire plane geometry. The track is an ideal line source that runs perpendicular to all wires, spans the transverse domain of the simulation, and is comprised of  $\approx 4400$  ionization electrons per mm mimicking a MIP. Only the field response and pre-amplifier electronics response ( $2\mu\text{s}$  peaking time and  $14\text{ mV}$  gain) are included; diffusion is neglected. “0 wire” depicts the signal for charge drifting within one-half pitch distance of a central wire. The “[ $-N,+N$ ] wire” plots provide the contribution to the signal on the central wire from ionization electrons that drift in progressively more distant  $N$  neighboring wire regions.

To describe the signal dependence on track topology and later for evaluation of the signal processing technique (section 4.3), the detector Cartesian coordinate as well as each wire plane's coordinate are defined.

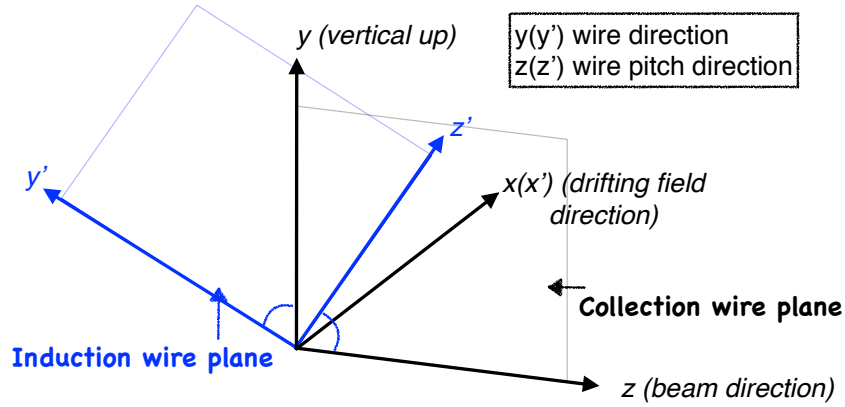
*Coordinate system for each wire plane* – As shown in figure 8a, for each wire plane, the  $x$ -axis is along the drifting field direction, the  $y$ -axis is along the wire orientation, and the  $z$ -axis is along the wire pitch direction. The nominal (default) detector coordinate system is identical to the collection plane's coordinate system for which the  $y$ -axis is vertical in the upwards direction and the  $z$ -axis is along the wire pitch direction.

*Angles for topology description* – Based on the predefined coordinate for each wire plane, two angles are defined as well to describe the topology of the track. As shown in figure 8b,  $\theta_y$  is the angle between the track and the  $y$ -axis, and  $\theta_{xz}$  is the angle between the projection onto the  $x - z$  plane and the  $z$ -axis.

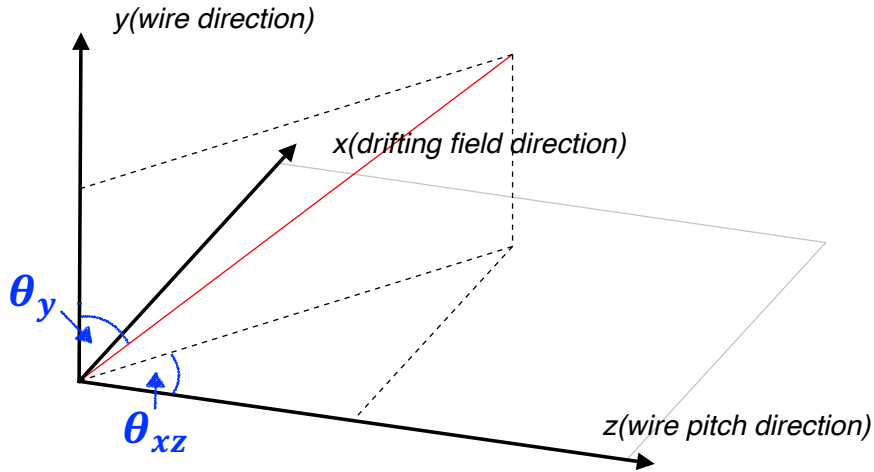
Since the  $x$  component determines the time extent of the track and the  $z$  component determines the range of sense wires (channels),  $\theta_{xz}$  alone determines the shape of the TPC signal, assuming the field response is identical along the  $y$ -axis (wire orientation). This assumption exactly holds in the current 2D field response calculation and corresponds to roughly the average of the 3D field response. The  $y$  component is proportional to the length of the charge deposition projection on the wire direction. It simply scales the charge deposition within one wire pitch by  $1/(\cos \theta_{xz} \cdot \sin \theta_y)$ . As an example, figure 9 and figure 10 demonstrate the TPC signal topology-dependency on  $\theta_{xz}$  and  $\theta_y$ . Note that the discussions above are related to the individual coordinates and angles for each wire plane. One track in the detector coordinate has different angles with respect to each wire plane's coordinate.

Compared to the collection plane signals, the induction plane signals can be much smaller due to the cancellation of the various bipolar signals from all nearby elements of an extended event topology. In particular, for a track traveling in a direction close to normal to the wire planes (commonly referred to as a *prolonged track*), its induction plane signals will have low amplitude and a long duration in time (figure 9). This amplitude can be comparable to noise levels. Having the lowest achievable inherent electronics noise [27], avoiding excess noise sources, and applying proper signal processing are crucial to resolve the induction plane signals. Recovering these signals enables new opportunities to take full advantage of the LArTPC's capability and reduce its residual ambiguities in later reconstruction. In order to minimize the inherent electronics noise, MicroBooNE uses a custom designed complementary metal-oxide-semiconductor (CMOS) analog front-end application-specific integrated circuit (ASIC) [28] operating at cryogenic temperatures inside the liquid argon. The close proximity of the preamplifier to the sense wire minimizes the input capacitance. The low temperature of LAr further reduces the electronics noise of the ASIC. The residual equivalent noise charge (ENC) after the software noise filtering varies with wire length and is found to be around 400 electrons for the longest wires (4.7 m) in MicroBooNE. This noise level is significantly lower than previous experiments utilizing warm front-end electronics. More details can be found in [27].





(a) Coordinates for collection and induction planes. The  $y'$  ( $z'$ ) axis is rotated by  $60^\circ$  around the  $x$  axis from the  $y$  ( $z$ ) axis. The illustrated induction plane's coordinate is consistent with the V plane's and the U plane's is with a rotation in the opposite direction.



(b) Definition of two angles,  $\theta_{xz}$  and  $\theta_y$ .

**Figure 8:** Geometric coordinates and angles for topology description.

### 3 Reconstruction of drifted electron distribution

In this section, we describe the principle for reconstructing the charge distribution of drifted ionization electrons (section 3.1) from the measured TPC signal waveform and the actual implementation of algorithms applied in analyzing MicroBooNE data (section 3.2).

#### 3.1 Signal extraction principles

As described in section 2, the raw digitized TPC signal is a convolution of the arriving ionization electron distribution, the field response describing the induced current on wires due to moving charge, and the overall electronics response. The goal of TPC charge extraction is to unfold the

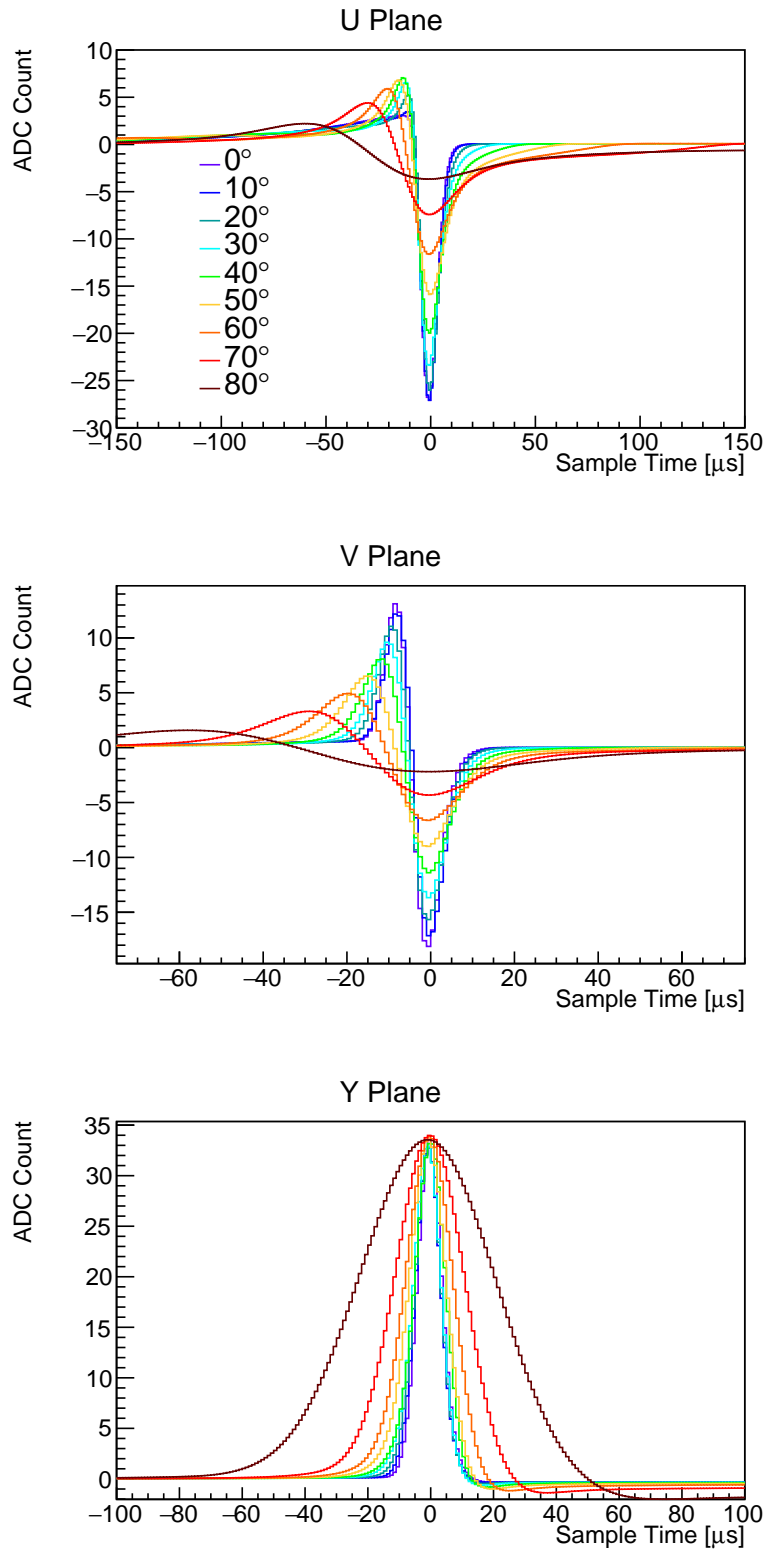


**Figure 9:** Simulated baseline-subtracted MicroBooNE TPC signals for a 1 meter long MIP track ( $\approx 4400$  ionization electrons per mm) traveling perpendicular to each wire plane orientation ( $\theta_y = 90^\circ$ ) with  $\theta_{xz}$  varying in the  $x - z$  plane with respect to the  $z$ -axis. Detector physics effects and the nominal MicroBooNE electronics response [19] were included. The signal shape is solely determined by  $\theta_{xz}$ , independent of  $\theta_y$ .

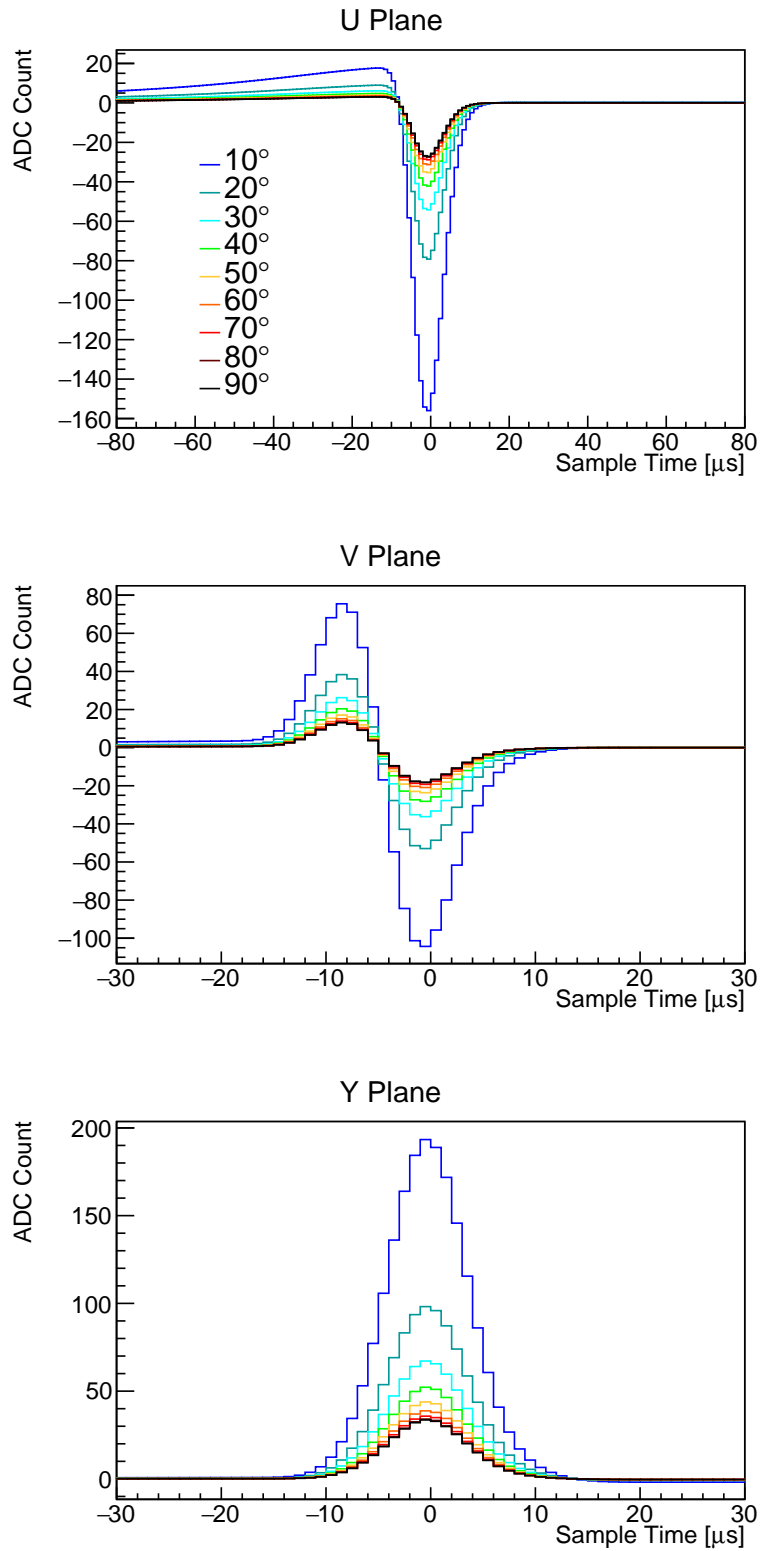


**Figure 10:** Simulated baseline-subtracted MicroBooNE TPC signals for a 1 meter long MIP track ( $\approx 4400$  ionization electrons per mm), isochronous ( $\theta_{xz} = 0^\circ$ ) with  $\theta_y$  varying with respect to the wire orientation. Detector physics effects and the nominal MicroBooNE electronics response [19] were included. Given a  $\theta_{xz}$ ,  $\theta_y$  just changes the signal amplitude.

field and electronics responses from the raw TPC signal and to recover the number of ionization electrons passing by each wire at each sampled time.

### 3.1.1 Deconvolution and software filters

The principal method to extract charge is deconvolution. This procedure in its one-dimensional (1D) form has been used in the data analysis of previous liquid argon experiments [29, 30]. This technique has the advantages of being robust and fast. It is an essential step in the overall drifted-charge profiling process.

Deconvolution is a mathematical technique to extract the *original signal*  $S(t)$  from the *measured signal*  $M(t')$ . The measured signal is modeled as a convolution integral over the original signal  $S(t)$  and a given detector *response function*  $R(t, t')$ , which gives the instantaneous portion of the measured signal at some time  $t'$  due to an element of original signal at time  $t$ :

$$M(t') = \int_{-\infty}^{\infty} R(t, t') \cdot S(t) dt. \quad (3.1)$$

If the detector response function is time-invariant, then  $R(t, t') \equiv R(t' - t)$  and we can solve the above equation by performing a Fourier transformation, yielding  $M(\omega) = R(\omega) \cdot S(\omega)$ , where  $\omega$  is in units of angular frequency. We can derive the signal in the frequency domain by taking the ratio of the measured signal and the given response function:

$$S(\omega) = \frac{M(\omega)}{R(\omega)}. \quad (3.2)$$

In principle, the original signal in the time domain  $S(t)$  can then be obtained by applying the inverse Fourier transformation from the frequency domain  $S(\omega)$ . However in practice, there are two intermixed complicating effects. First, the measured signal  $M(t')$  contains an additional contribution from various electronics noise sources [27]. Second, in realistic detectors, the response function  $R$  decreases substantially at high frequency (large  $\omega$ ). These two factors lead to high-frequency components of the noise spectrum being artificially amplified through equation 3.2. If left unchecked, the derived signal  $S(\omega)$  would be completely overwhelmed by noise. To address this issue, a *filter function*  $F(\omega)$  is introduced, yielding

$$S(\omega) = \frac{M(\omega)}{R(\omega)} \cdot F(\omega). \quad (3.3)$$

Its purpose is to attenuate the problematic high frequency noise. The addition of the filter function  $F$  can be considered as a replacement of the response function  $R$ . In essence, the deconvolution replaces the real field and electronics response function with an effective software filter response function. The advantage of this procedure is most pronounced on the induction plane where the irregular bipolar field response function is replaced by a regular unipolar response function through the inclusion of the software filter.

A common choice of software filter is the Wiener filter<sup>3</sup> [32], which is based on the expected signal  $\overline{S^2(\omega)}$  and noise  $\overline{N^2(\omega)}$  frequency spectra:

$$F(\omega) = \frac{\overline{R^2(\omega)S^2(\omega)}}{\overline{R^2(\omega)S^2(\omega)} + \overline{N^2(\omega)}}. \quad (3.4)$$

---

<sup>3</sup>A discussion of the application of the Wiener filter in the data unfolding problem can be found in [31].

With this construction, the Wiener filter is expected to achieve the best signal to noise ratio with minimal mean square error (the sum of the variance and the squared bias) of the deconvolved distribution. However, naively applying the Wiener filter to TPC signal processing is problematic for three reasons. Firstly, as described in section 2.3, the TPC signal  $S(\omega)$  varies substantially depending on the exact nature of the event topology. The electronics noise spectrum is also a function of the duration of the time window over which it is observed. A longer time window allows for observation of more low frequency noise components. Therefore, it is impractical to achieve a universal Wiener filter yielding the best signal-to-noise ratio for all signals of varying time windows. Secondly, given the definition of the Wiener filter in equation 3.4, we have  $F(\omega = 0) < 1$ . Considering the addition of the filter as a replacement of the response function  $R(t' - t)$ , we can see that the Wiener filter does not conserve the total number of ionization electrons. Thirdly, as shown in equation 3.3, the filter acts as a replaced response function and smears the extracted ionization electron distribution along the drift time dimension. Since the drift time is equivalent to the drift distance, a filter that can alter the charge distribution in an extended (non-local) time range instead of in a short (local) one is undesirable. For induction wire planes, none of the ionization electrons are expected to be collected, which leads to a bipolar signal in the time domain and a low-frequency suppressed signal in the frequency domain. A direct construction of the Wiener filter with this low-frequency suppression would lead to a non-local charge smearing. To overcome these shortcomings associated with the Wiener filter, we use a Wiener-inspired filter. Details are elaborated upon in section 3.2.2.

### 3.1.2 2D deconvolution

As described in section 2, the induced current on the sense wire receives contributions not only from ionization charge passing by the sense wire, but also from ionization charge drifting in nearby wire regions. Naturally, the contribution of charge farther from the target sense wire is smaller. Ignoring the variation of the strength of the field response within one wire region, equation (3.1) can be expanded to

$$M_i(t_0) = \int_{-\infty}^{\infty} (\dots + R_1(t_0 - t) \cdot S_{i-1}(t) + R_0(t_0 - t) \cdot S_i(t) + R_1(t_0 - t) \cdot S_{i+1}(t) + \dots) \cdot dt, \quad (3.5)$$

where  $M_i$  represents the measured signal from wire  $i$ .  $S_{i-1}$ ,  $S_i$ , and  $S_{i+1}$  represent the real signal inside the boundaries of wire  $i$  and its adjacent neighbors.  $R_0$  represents an average response function for an ionization charge passing through the wire region of interest. The average is taken over all possible drift paths through the wire region. Similarly,  $R_1$  represents the average response function for an ionization charge drifting past in the next adjacent wire region. One can expand this definition to  $n$  number of neighbors by introducing terms up to  $R_n$ . Equation (3.5) assumes translational invariance in the response function (i.e. the  $R$  does not depend on the actual location of the wire). In section 4.2.5, we will discuss the impact of ignoring position dependence of the field response at small scales within the wire region of interest.

If we then apply a Fourier transform on both sides of equation (3.5), we have:

$$M_i(\omega) = \dots + R_1(\omega) \cdot S_{i-1}(\omega) + R_0(\omega) \cdot S_i(\omega) + R_1(\omega) \cdot S_{i+1}(\omega) + \dots, \quad (3.6)$$

which can be written in matrix notation as:

$$\begin{pmatrix} M_1(\omega) \\ M_2(\omega) \\ \vdots \\ M_{n-1}(\omega) \\ M_n(\omega) \end{pmatrix} = \begin{pmatrix} R_0(\omega) & R_1(\omega) & \dots & R_{n-2}(\omega) & R_{n-1}(\omega) \\ R_1(\omega) & R_0(\omega) & \dots & R_{n-3}(\omega) & R_{n-2}(\omega) \\ \vdots & \vdots & \ddots & \vdots & \vdots \\ R_{n-2}(\omega) & R_{n-3}(\omega) & \dots & R_0(\omega) & R_1(\omega) \\ R_{n-1}(\omega) & R_{n-2}(\omega) & \dots & R_1(\omega) & R_0(\omega) \end{pmatrix} \cdot \begin{pmatrix} S_1(\omega) \\ S_2(\omega) \\ \vdots \\ S_{n-1}(\omega) \\ S_n(\omega) \end{pmatrix} \quad (3.7)$$

Now, if we assume that we know all response functions (i.e. the matrix  $R$ ), the problem converts into deducing the vector  $S$  from the measured signal  $M$  by an inversion of matrix  $R$ , provided that the wires of interest are distant from the wire plane edges, the matrix  $R$  is symmetric and Toeplitz<sup>4</sup>, and the inverse problem can be solved using discrete-space Fourier transformation techniques as discussed in section 3.1.1, on  $M_i(\omega)$ ,  $S_i(\omega)$ , and  $R_i(\omega)$ . Therefore, instead of 1D a deconvolution involving only the time dimension, a two-dimensional (2D) deconvolution involving both time and wire dimensions is performed to recover the ionization electron distribution. An additional Wiener-inspired filter is applied to the wire dimension deconvolution in analogy to that of the time domain deconvolution. These software filters will be discussed in section 3.2.2.

An example comparison of the 1D and 2D deconvolution results in a data event can be seen in figure 11, demonstrating the charge recovery using the 2D deconvolution approach in contrast to the 1D method. Figure 11 highlights the signal dependence on topology and long range induction. An evaluation of 2D deconvolution signal processing performance given the topological dependence of the signal and the long range induction inherent to the signal is considered in section 4.

### 3.1.3 Region of interest (ROI)

The 2D deconvolution procedure described in section 3.1.2 provides a robust and computationally-efficient method to extract the distribution of ionization electrons. While successful for the collection plane the procedure is still not optimal for the induction planes due to the bipolar nature of the measured induction plane signals. In order to illustrate this point, the average response functions on the closest wire for a point-like ionization charge is shown in figure 12. The average response function includes both the average field response (averaged over all possible electron drift paths within the wire region as simulated by Garfield without diffusion) and the electronics response (2  $\mu$ s peaking time). The normalization of the overall response function is chosen so that the integral of the collection plane response function is unity, corresponding to a single electron. Figure 12b shows the frequency components of the average response functions for the three wire planes. All responses have suppressions at high frequency, where the filter is required to stabilize the deconvolved results (e.g. equation 3.3). Compared to the collection wire response, the induction wire responses exhibit suppressions at low frequency. In particular, at zero frequency, the frequency components are equivalent to the integral of the response function over time and should be close to zero as indicated by equation 2.4.

Similar to the situation at high frequencies, the suppression of the induction responses at low frequencies is problematic for the proposed deconvolution procedure. As shown in [27],

---

<sup>4</sup>A Toeplitz matrix is one for which each diagonal descending from left to right has all elements equal. Multiplication by a Toeplitz matrix is equivalent to an operation of discrete convolution.

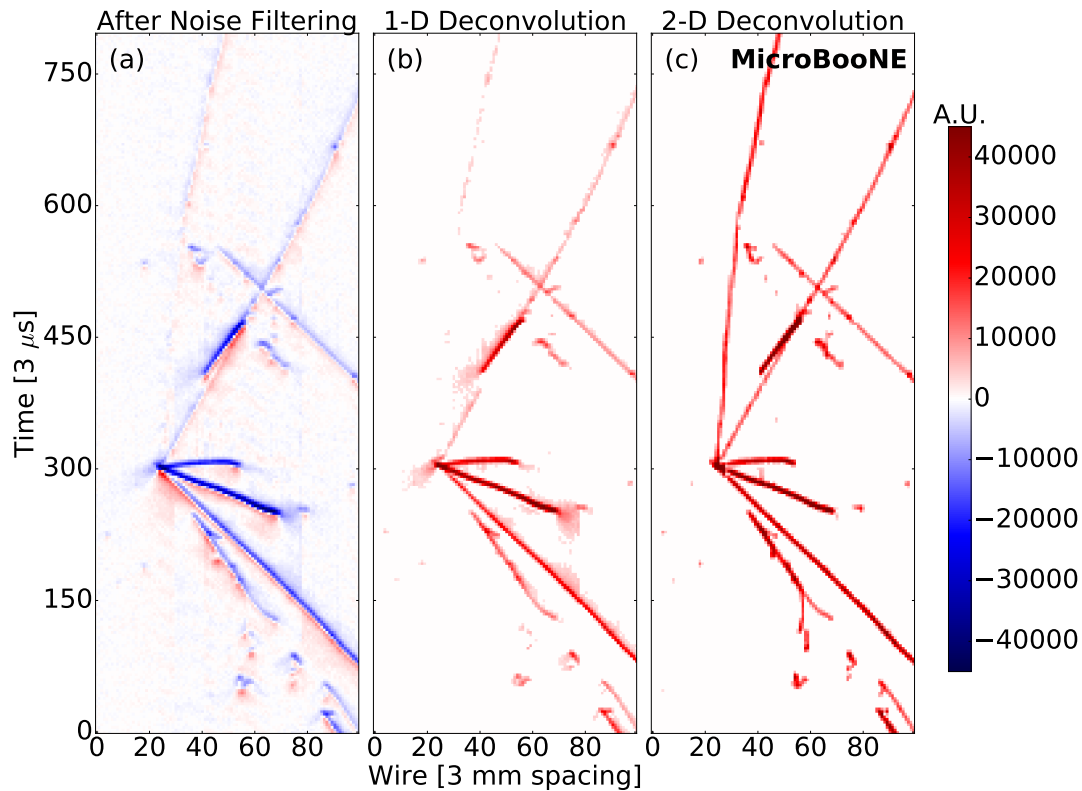
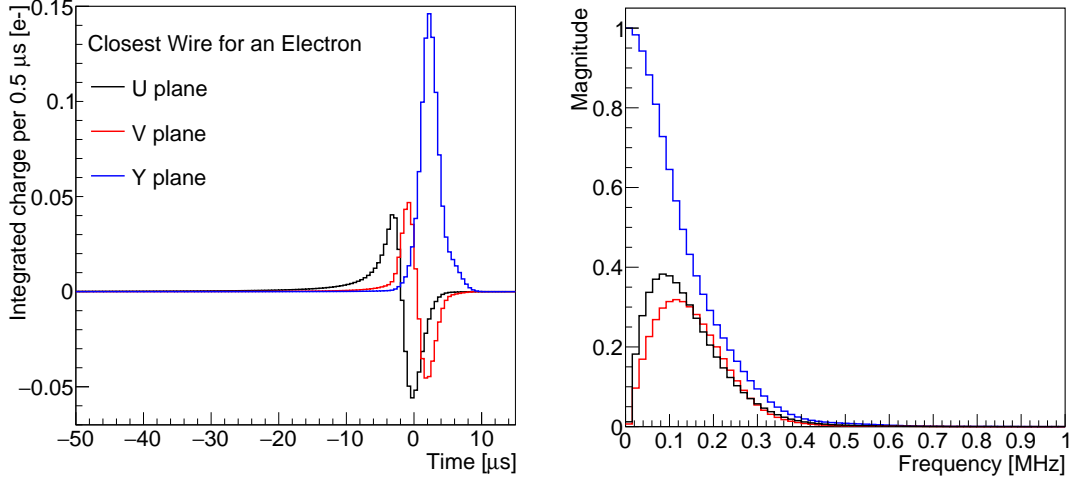


**Figure 11:** A neutrino candidate from MicroBooNE data (event 41075, run 3493) measured on the U plane. (a) Raw waveform after noise filtering in units of average baseline subtracted ADC scaled by 250 per  $3 \mu\text{s}$ . (b) Charge spectrum in units of electrons per  $3 \mu\text{s}$  after signal processing with 1D deconvolution. (c) Charge spectrum in units of electrons per  $3 \mu\text{s}$  after signal processing with 2D deconvolution.

the measured signal contains electronics noise, which is not necessarily as suppressed at low frequencies. Therefore, following equation (3.3), the low frequency noise will be amplified in the deconvolution process. The amplification of low frequency noise can be seen clearly in figure 18a. Left unmitigated, the amplification of low frequency noise would lead to an unacceptable uncertainty in the charge estimation.

In principle, the amplification of the low-frequency noise through the deconvolution process can be suppressed through the application of low-frequency (high-pass) filters similar to the filters suppressing high-frequency (low-pass) noise. However, as explained in section 3.1.1, applying such a low-frequency filter would lead to an alteration of the charge distribution in extended (non-local) time ranges, which is not desirable. Instead we turn to the technique of selecting a signal region of interest (ROI) in the time domain.

The region of interest (ROI) technique was proposed [30] to reduce the data size and to speed up the deconvolution process. The idea is to limit the deconvolution to a small time window that is slightly bigger than the extent of the signal it contains. The entire event readout window (4.8 ms for MicroBooNE) is replaced by a set of ROIs. For induction wire signals, the ROI technique also



(a) Average response in time domain. (b) Average response in frequency domain.

**Figure 12:** Examples of simulated average response functions for induction (black and red) and collection (blue) wires in the time (a) and frequency (b) domains.

limits the low frequency noise. To illustrate this point, we consider a time window with  $N$  samples. MicroBooNE samples at intervals of  $0.5 \mu\text{s}$  and the highest frequency that can be resolved is the Nyquist frequency of 1 MHz. After a discrete Fourier transform, the bin above the first bin (zero frequency) starts at  $\frac{1\text{MHz}}{N/2}$ . The noise in the zero-frequency bin represents a baseline shift after the ROI is transformed back into the time domain. Therefore, once we identify the signal region and create a ROI just big enough to cover the signal, we can naturally suppress the low-frequency noise at the cost of having to correct for the baseline shift. This correction is performed through a linear interpolation of the two baselines, determined by samples at the start and end of the ROI window in the time domain.

### 3.2 Method

In this section, we describe the inputs and the detailed algorithms to extract the ionization charge spectrum from the digitized TPC wire plane signals, based on the principles described above. The algorithm is implemented and available at [33].

In general, the full chain contains four major steps:

- **Noise filtering:**  
Apply specific noise filters to remove possible excess noise apart from the inherent electronics noise. The results of this step have been previously reported in [27].
- **2D deconvolution:**  
Apply a 2D deconvolution to the digitized TPC wire signals, resulting in a deconvolved charge distribution. An average field response involving multiple sense wires is calculated and utilized as shown in section 3.2.1. Two types of deconvolved charge spectra are obtained, corresponding to different software filters for the time domain. A Wiener-inspired filter is



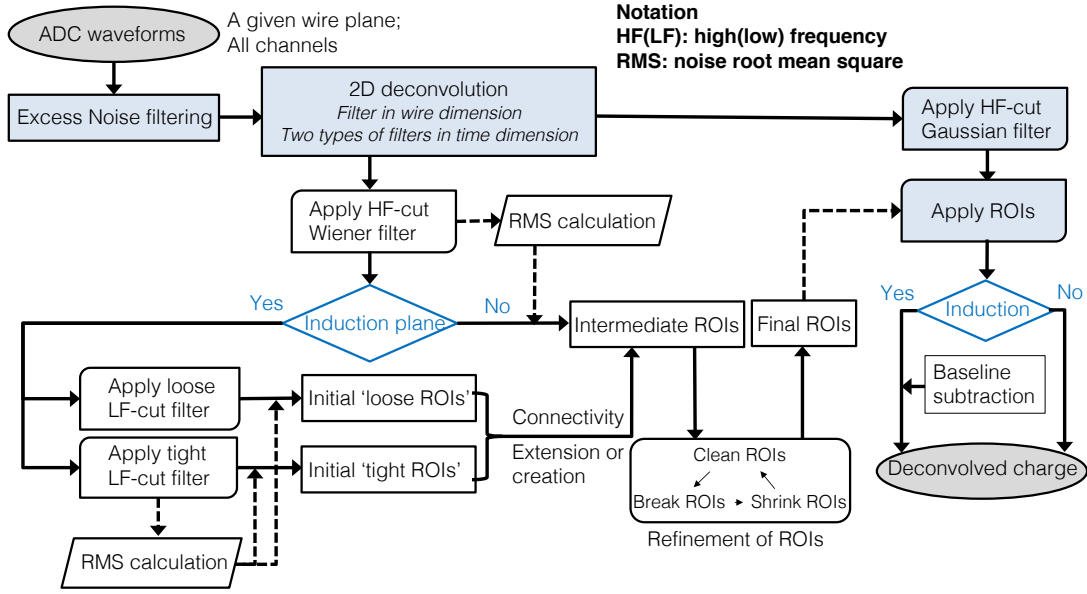


**Figure 13:** A flow chart of the full chain of signal processing. See text for explanation.

applied to maximize the signal-to-noise ratio with better time resolution and a Gaussian filter is applied to achieve a non-distorted charge spectrum except for a Gaussian smearing. Details will be explained in section 3.2.2.

- **ROI finding and refining:**

Perform ROI finding with the deconvolved charge distribution after the Wiener-inspired filter. The principle of these algorithms will be explained in section 3.2.3 and 3.2.4. In short, loose and tight high-pass filters are combined to optimize the purity and efficiency of ROI finding.

- **ROI application:**

Apply the identified ROI window to the deconvolved charge distribution after the Gaussian filter and extract the ionization charge, with a linear baseline subtraction for the induction planes based on the start/end bins of the ROI window.

A flow chart of the full chain of the aforementioned signal processing can be seen in figure 13.

### 3.2.1 Position-averaged response functions

Since the signal in a readout wire is recorded without any prior knowledge of the transverse position distribution of electrons within a wire region, the average response functions are used in the 2D deconvolution as discussed in section 3.1.2. The average response function for a single electron within a particular wire region is obtained through the following summation:

$$R_i = \frac{0.5 \times R_i^{0.0 \text{ mm}} + R_i^{0.3 \text{ mm}} + R_i^{0.6 \text{ mm}} + R_i^{0.9 \text{ mm}} + R_i^{1.2 \text{ mm}} + 0.5 \times R_i^{1.5 \text{ mm}}}{5}, \quad (3.8)$$

where  $R_i^z$  represents the response function at the  $i$ th wire for an electron starting at  $z$  transverse position. The impact of applying the average response function in the 2D deconvolution will be

explained in section 4.2.5. These average responses for 21 wires (the central wire  $\pm 10$  wires on both sides) are shown in figure 14. The left panel shows the response function in 2D with the “Log10” scale. The X-axis represents the wire number. The Y-axis represents the drift time with 1 tick of  $0.5 \mu\text{s}$  in each bin. The normalization is the same as that in figure 4. The right panel shows the average response function in a linear scale for the first five wires. For the V and Y wire planes, the strength of the response function drops quickly for wires further away from the central wire (i.e. negligible beyond  $\pm 4$  wires). For the U induction wire plane, the strength of the response function is still sizable at  $\pm 4$  wires. This is due to the fact that the U induction wire plane is the first wire plane facing the active TPC volume without any shielding.

### 3.2.2 Software filters

In this section, we describe the derivation of the software filters used in the signal processing. As mentioned in section 3.1.1, the chosen Wiener-inspired filter is based on the Wiener filter in equation 3.4 constructed from simulation. The time window is chosen to be  $100 \mu\text{s}$  which generally performs well in a variety of cases with proper additional smearing of the signal. The signal is chosen to be an isochronous MIP track traveling perpendicular to the wire orientation. The total number of ionization electrons is assumed to be  $1.6 \times 10^4$  per wire pitch. The RMS of the spread in the drift time due to diffusion is taken to be 1 mm, corresponding to the average drift distance in the MicroBooNE detector. The gain and peaking time are 14 mV/fC and  $2 \mu\text{s}$ , which is the same as the nominal running condition [27]. The electronic noise is simulated in an analytic way, as will be described in section 4.2.6. The results following equation (3.4) were then fitted with the following functional form in order to exclude low-frequency suppressions presented in the original Wiener filters:

$$F(\omega) = c \cdot e^{-\frac{1}{2} \cdot \left(\frac{\omega}{a}\right)^b}, \quad (3.9)$$

where  $a$ ,  $b$ ,  $c$  are free parameters to be determined by the fit. This functional form of the filter guarantees that the corresponding smearing function (filter) in the time domain is local. Given the fit, the filter is chosen to be

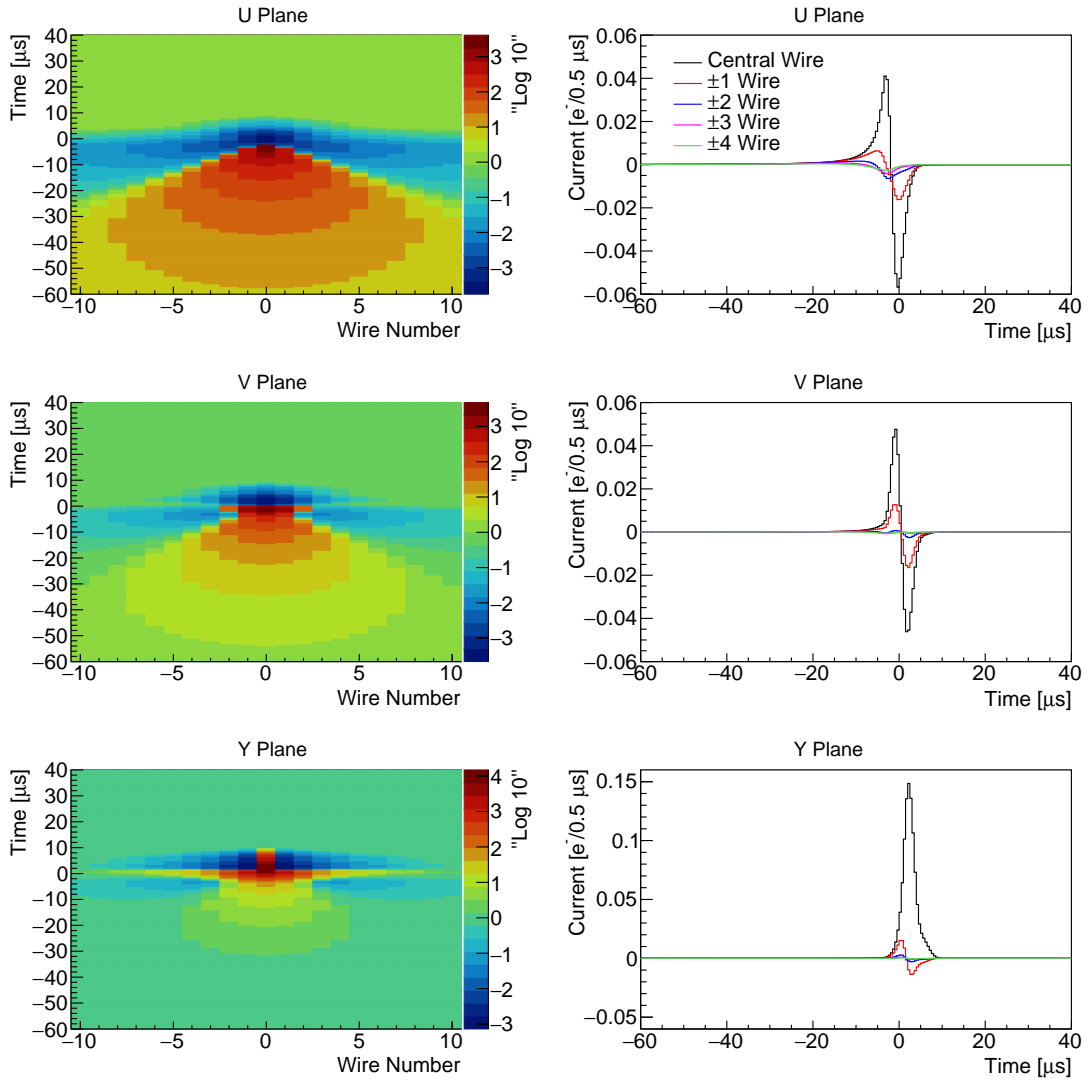
$$F(\omega) = \begin{cases} e^{-\frac{1}{2} \cdot \left(\frac{\omega}{a}\right)^b} & \omega > 0 \\ 0 & \omega = 0, \end{cases} \quad (3.10)$$

with  $a$  and  $b$  being the same parameters as in equation 3.9 with  $c$  removed. The modification of the filter takes into account the following considerations:

- The filter is explicitly zero at  $\omega = 0$  in order to remove any DC component in the deconvolved signal. This removes information about the baseline. A new baseline is calculated and restored for the waveform after deconvolution.
- The above functional form of the filter leads to

$$\lim_{\omega \rightarrow 0} F(\omega) = 1. \quad (3.11)$$

This means that the integral of the corresponding smearing function in the time domain is unity, which does not introduce any extra factor in the overall normalization.



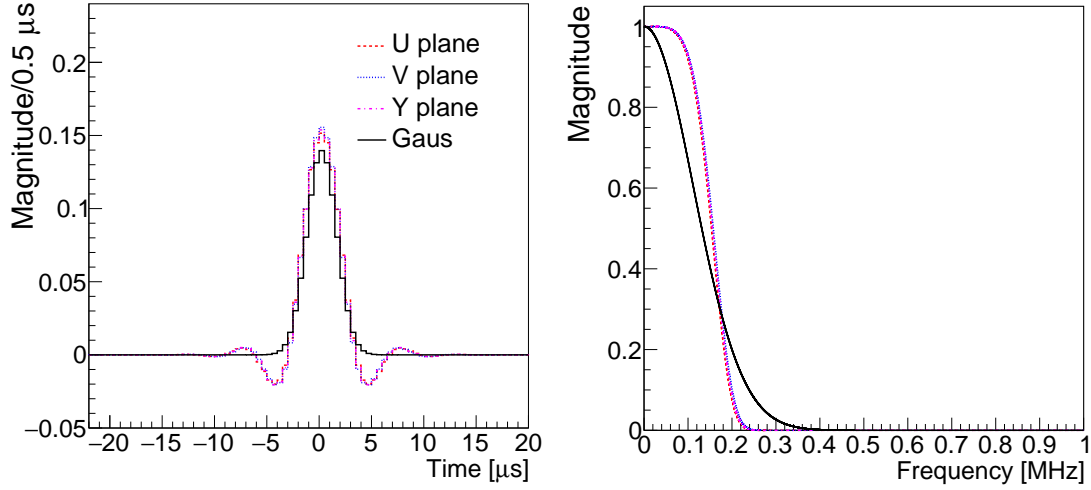
(a) Wire number versus time in “Log10” scale. (b) Response functions for each of the first five wires.

**Figure 14:** The position-averaged response functions after convolving the field response function and an electronics response function at 2 μs peaking time in “Log 10” scale (a) and linear scale for the first 5 wires (b).

Figure 15 shows the three Wiener-inspired filters and a Gaussian filter,

$$F(\omega) = \begin{cases} e^{-\frac{1}{2} \cdot (\frac{\omega}{a})^2} & \omega > 0 \\ 0 & \omega = 0, \end{cases} \quad (3.12)$$

for charge extraction. Compared to the Wiener-inspired filters, the Gaussian filter is expected to have a slightly worse signal-to-noise ratio. However, such a filter has advantages in calculating the charge and is better matched with a Gaussian hit finder that may be used in later stages of event



(a) Filters in the time domain.

(b) Filters in the frequency domain.

**Figure 15:** Wiener-inspired (dashed line) and Gaussian (solid line) software filters are shown in (a) the time domain and (b) the frequency domain for each of the three wire planes. In the time domain, we commonly refer to the filter function as the smearing function. With the chosen functional forms, the local behavior of the filters is apparent from their shapes.

reconstruction.

In 2D deconvolution, a similar filter in the wire dimension is constructed using the Gaussian form

$$F(\omega_w) = e^{-\frac{1}{2} \cdot \left(\frac{\omega_w}{a}\right)^2} \quad (3.13)$$

where the “frequency”,  $\omega_w$ , is the Fourier transform over the wire number instead of time. Figure 16 shows the filters in the wire domain. Different parameters are chosen for induction and collection wire planes.

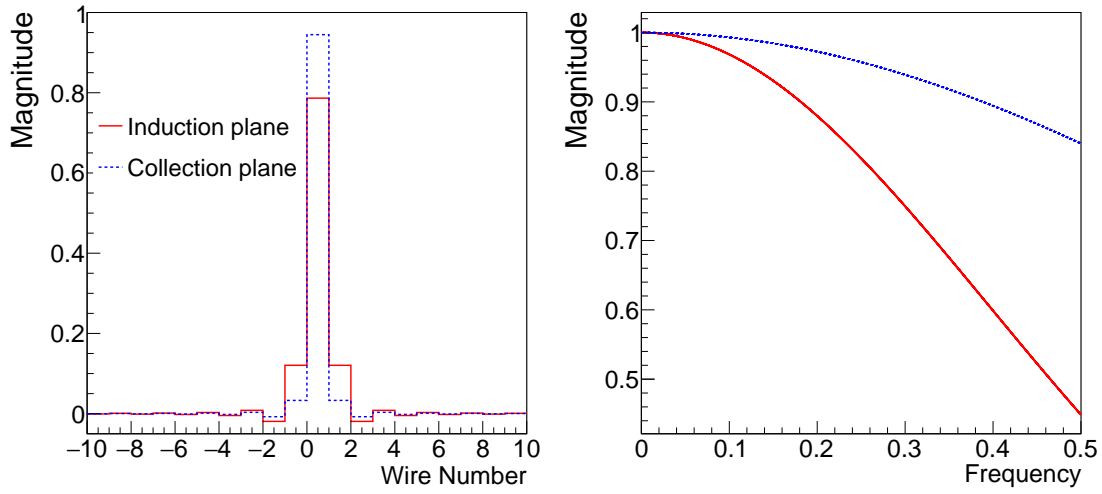
### 3.2.3 Identification of signal ROIs

As shown in figure 18a, the direct application of the deconvolution procedure significantly amplifies the low-frequency noise for the induction wire planes. In order to identify the signal regions of interest (signal ROIs or ROIs for short), additional low-frequency filters with a functional form

$$F_{LF}(\omega) = 1 - e^{\left(\frac{\omega}{a}\right)^2}, \quad (3.14)$$

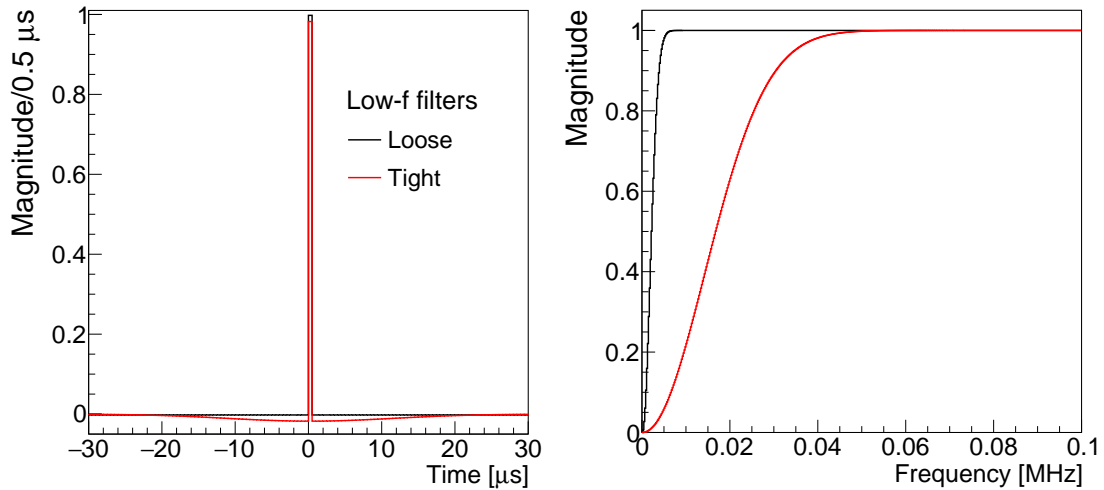
are applied to the deconvolved charge distribution for the induction wire planes to search for ROIs. These low-frequency filters are not used for the collection wire plane signal.

Figure 17 shows the two low-frequency filters used to identify ROIs for induction wire planes. Due to suppressions at low frequencies, the corresponding smearing functions in the time domain exhibit a long negative tail. The magnitude of the negative tail is larger for the tight low-frequency filter, whereas the tail extends to longer times for the loose low-frequency filter. Since such a long-range behavior is not desired for the filters used to obtain the charge signal, these filters are exclusively used to identify ROIs.



(a) Wire filters in the wire number domain. (b) Wire filters in the “frequency” domain.

**Figure 16:** Filters using a Gaussian form are applied for the wire dimension shown in both the wire number (a) and “frequency” (b) domains. Different parameters are chosen for induction and collection wire planes.



(a) Low-frequency filters in the time domain. (b) Low-frequency filters in the frequency domain.

**Figure 17:** Low-frequency filters used in identifying ROIs for induction wire planes shown in both the time (a) and frequency (b) domains.

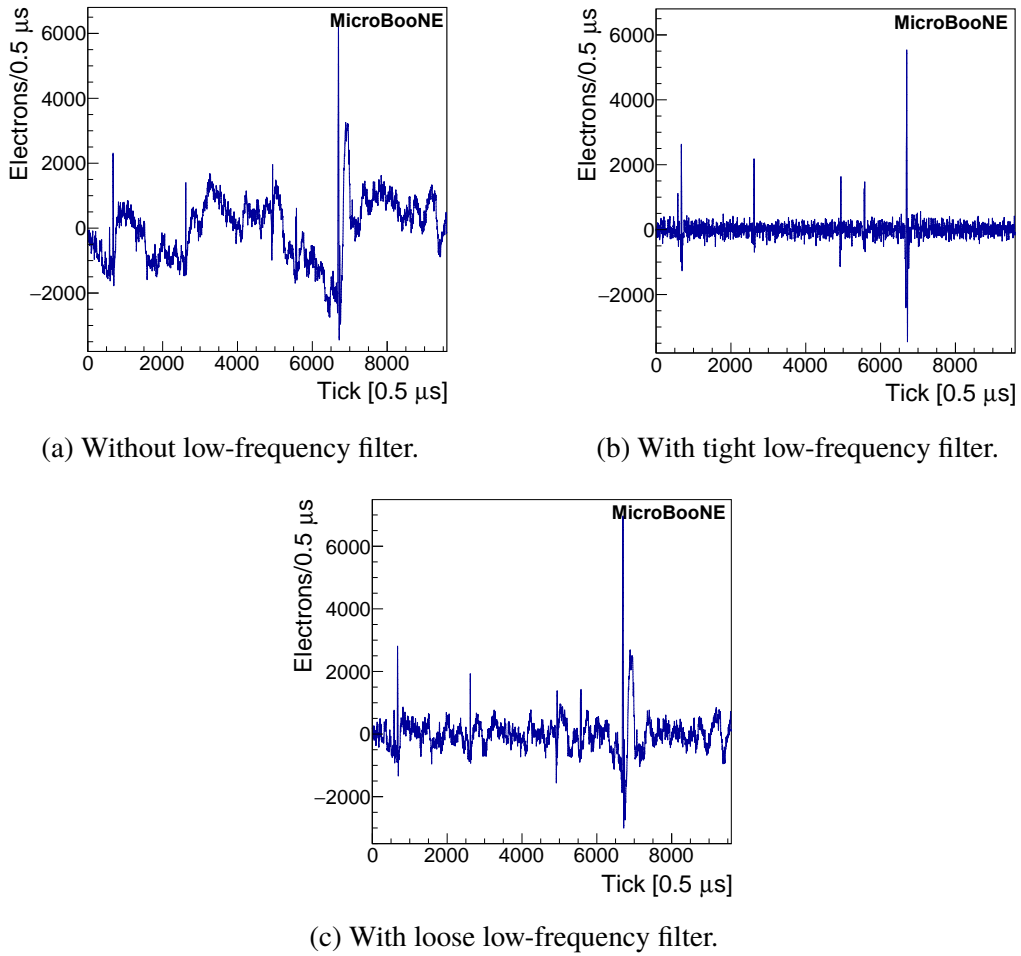


**Figure 18:** Comparison of the deconvolved signal on the U induction plane (a) without the low-frequency filter, (b) with the tight low-frequency filter, and (c) with the loose low-frequency filter.

Figure 18 shows the impact of these low-frequency filters. Without the filter, the low-frequency noise totally overwhelms the signal (figure 18a). After applying the tight low-frequency filter (figure 18b), the signal-to-noise ratio improves for short (in time) signals. However, the long signal at around 7000 time ticks is removed by the tight low-frequency filter. It is recovered by the loose low-frequency filter (figure 18c).

The deconvolved charge distribution for each channel within the entire readout window ( $\sim 9600$  ticks) is used to calculate the RMS (root mean square) noise, to set the threshold of the ROI identification. The RMS is calculated using a 68% quantile range relative to the ADC count distribution mean value. This RMS calculation is insensitive to the true signals in the deconvolved charge distribution. For the collection plane, the threshold is set at 5 times the RMS noise which is about 300 electrons/tick on average. For the induction planes, the deconvolved charge distribution with the tight low-frequency filter is employed to calculate the RMS noise and the threshold is set at 3.5 times the RMS noise, which is about 350 electrons/tick and 500 electrons/tick on average for the U plane and V plane, respectively.

ROIs are then extracted from these deconvolved signals. For the induction wire planes, there are two types of ROIs: tight and loose ROIs, which are extracted from the deconvolved signal after applying tight and loose low-frequency filters, respectively. The goal of the tight ROIs is to achieve high purity in terms of containing real signal. However, it is expected that tight ROIs have a low efficiency, in particular for long (in time) signals. On the other hand, the goal of the loose ROIs is to achieve high efficiency in terms of containing real signal. The trade-off is that we expect the purity of the loose ROIs to be lower. ROIs are then extracted by searching for signal above noise. Each ROI is then extended in time to cover the signal tails. For (ROIs) tight ROIs in the (collection) induction plane, additional ROIs are created by examining the connectivity of the existing ones. Each of the loose ROIs is then compared with the tight ROIs on the same wire. If one loose ROI overlaps with a tight ROI, the loose ROI is extended to ensure the tight ROI is contained. If a tight ROI is not contained by a loose ROI, a new loose ROI with the exact range of the tight ROI is created. The operations above ensure that each tight ROI is contained by a loose ROI. Figure 19 shows the impact of including tight and loose ROIs for the induction plane signal processing.

### 3.2.4 Refinement of ROIs

As explained previously, the loose ROIs for the induction wire plane are expected to have a high efficiency in containing the real signal, but low purity. Therefore, an additional refining procedure using connectivity information is applied to exclude fake ROIs. The applicability of this methodology to a variety of event topologies demonstrates its robustness.

The basic components of the ROI refinement include:

- **Clean ROIs:**

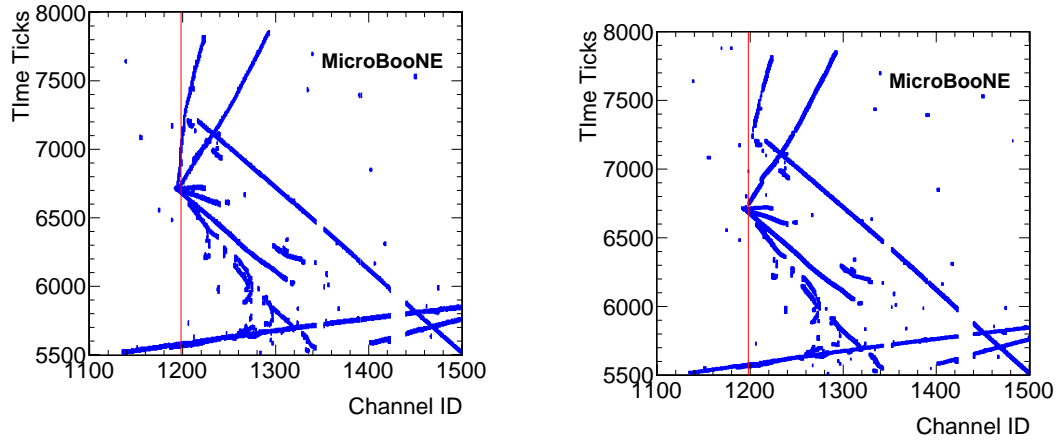
The motivation of this step is to remove fake ROIs—ROIs containing no signal. In particular, each loose and tight ROI is examined to ensure that part of the bin content inside the ROI is above a predefined threshold. ROIs failing this examination are removed. Loose ROIs are clustered according to connectivity information. For each loose ROI cluster, if none of its loose ROIs contain one or more tight ROIs, the cluster is removed entirely.

- **Break ROIs:**

The motivation of this step is to separate a loose ROI into a few small ROIs. Sometimes a few separated tracks (e.g. near the neutrino interaction vertex) can be quite close to each other along the drift time direction. Often a single loose ROI would be created to contain these tracks given the presence of low-frequency noise. Therefore, a special algorithm is needed to identify this scenario and separate the ROIs. In particular, each loose ROI is examined to search for multiple independent peaks. If found, the loose ROI is separated into several loose ROIs. Figure 20 shows the impact of the “break ROIs” step.

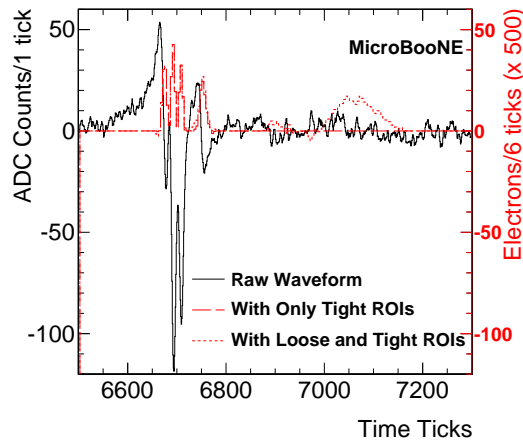
- **Shrink ROIs:**

The motivation of this step is to reduce the length of a ROI that contains real signal that had otherwise been accidentally extended into a much broader time range due to the presence of low-frequency noise. In particular, the range of each loose ROI is reduced according to the tight ROIs they contain as well as those in the adjacent loose ROIs. Figure 21 shows the effect of the “shrink ROIs” step.



(a) Deconvolved signal with “loose and tight ROIs”.

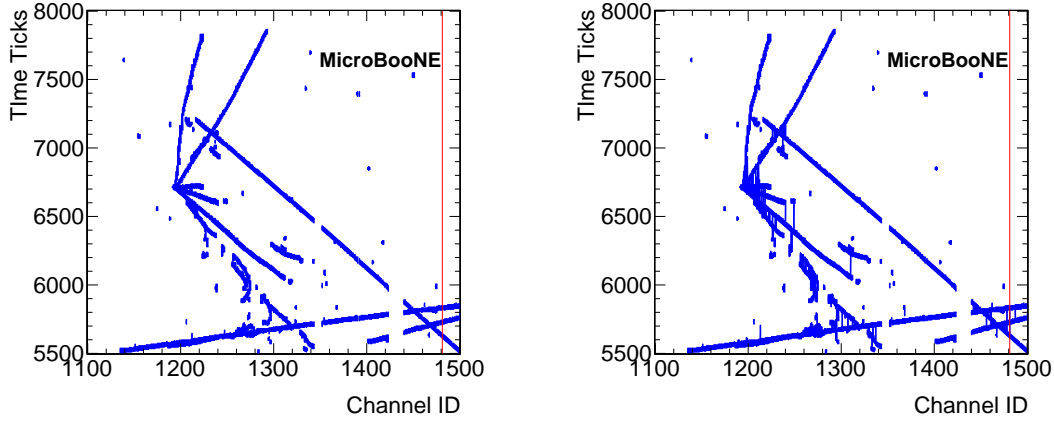
(b) Deconvolved signal with “tight ROIs”.



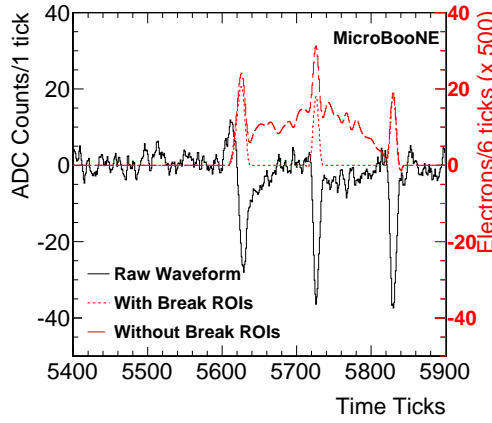
(c) Waveform comparison for the channel marked with a red line in (a) and (b).

**Figure 19:** A neutrino candidate from MicroBooNE data (event 41075, run 3493) on the U plane is shown in an event display with (a) and without (b) “loose ROIs”. In (c), the raw baseline-subtracted waveform (black) and the deconvolved signal with (dotted red) and without (dashed red) “loose ROIs” are presented.





(a) Deconvolved signal with “break ROIs”. (b) Deconvolved signal without “break ROIs”.



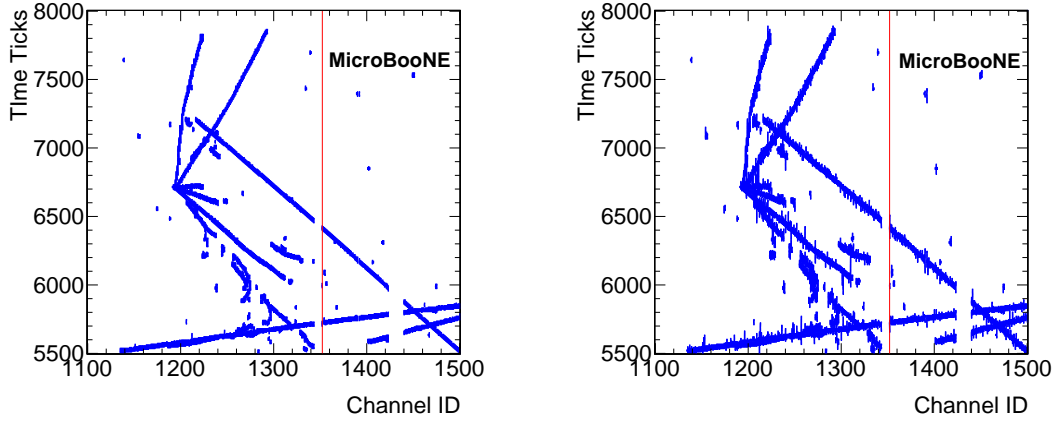
(c) Waveform comparison for the channel marked with a red line in (a) and (b).

**Figure 20:** The same neutrino candidate from figure 19 is shown in an event display with (a) and without (b) “break ROIs”. In (c), the raw baseline-subtracted waveform (black) and the deconvolved signal with (dotted red) and without (dashed red) “break ROIs” are presented.

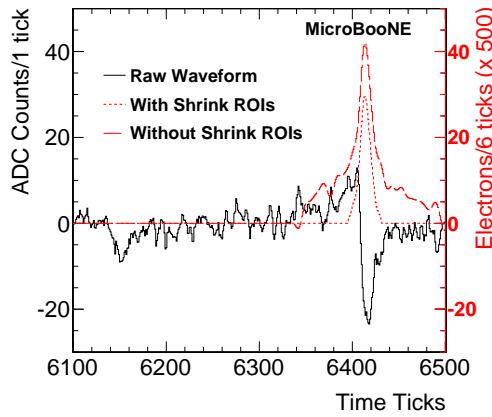
The overall ROI refinement takes an iterative approach by applying the above steps in sequence. The final remaining ROIs are then applied to the deconvolved signal without the low-frequency filter. A linear correction to the baseline is applied so that the bin content of the ROI boundaries are exactly zero.

#### 4 Evaluating TPC signal processing with simulation

This section describes the quantitative evaluation of the TPC signal processing using simulation. First, we describe some key improvements in the simulation. Next, the details of the simulation algorithms are shown. Finally, a quantitative evaluation of the signal processing using this simulation



(a) Deconvolved signal with “shrink ROIs”. (b) Deconvolved signal without “shrink ROIs”.



(c) Waveform comparison for channel marked with red line in (a) and (b).

**Figure 21:** The same neutrino candidate from figure 19 is shown in an event display with (a) and without (b) “shrink ROIs”. In (c), the raw baseline-subtracted waveform (black) and the deconvolved signal with (dotted red) and without (dashed red) “shrink ROIs” are presented.

is demonstrated including measures of reconstructed charge resolution, bias, and efficiency. The simulation itself is validated against MicroBooNE detector data in [19].

#### 4.1 Key simulation improvements

Evaluation of the signal processing relies, in part, on an improved signal and noise simulation. The signal simulation has two key improvements compared to prior implementations.

Previous implementations [34] adopted a simplified model to consider the induction charge from all drifting electrons, in which case the field response was extracted from an entire track at a single angle. An additional simplification was made to use a common, average field response

independent of the transverse distance between the wire and the drifting charge.

The improved simulation addresses these two issues by employing the field response calculations described in section 2.1. It supports a long-range induction model that more correctly incorporates angle-dependent effects and records the current induced not only on the closest wire but also current which is induced from the ten wires to either side. This allows for the accounting of contributions to the total induced current down to the sub-percent level. The simulation also takes into consideration the fine-grained variability that exists for different possible paths within a single wire region.

The second improvement relates to the treatment of the complexity inherent in the initial distribution of energy depositions by particles interacting in the LAr and its resulting distribution of ionization electrons. In past implementations, the ionization electrons were grouped into spatial bins and the contribution to induced current was extracted from each bin. To improve on this, the new simulation retains the identity of each energy deposition produced by a given step of the particle tracking simulation. The effects of diffusion and absorption are applied to each ionization point by associating a 2D Gaussian charge distribution. The distributions for all ionization points are kept distinct during drifting until they reach the wire planes. There, they are sampled and interpolated onto the regular 2D grid defined in the transverse and longitudinal directions by the field response functions described in section 2.1. At this point, a fine binning ( $0.5 \mu\text{s} \times 0.3 \text{ mm}$  for the MicroBooNE implementation) is applied.

The simulation improvements described above highlight an important connection between the choice of signal simulation and the signal processing models which may be employed. The former primarily applies a convolution of the ionization charge distribution and the field (and electronics) response functions. The latter primarily performs their deconvolution. Prior simulation implementations used the same kernel in both the convolution and deconvolution processes. In the absence of noise and up to the spatial binning simulated, the prior simulation approach produces an exact recovery of the initial ionization charge distribution, which is not representative of real detector effects. The new approach supports a better approximation of reality by allowing the variation of field response across a wire region to be accounted for in the convolution. However, this variation cannot be accounted for in the deconvolution as there exists no *a priori* knowledge of the fine-grained charge distribution. Quantification of this effect, i.e. the realistic performance of signal processing, is one of the goals of the evaluation shown here.

## 4.2 Simulation overview

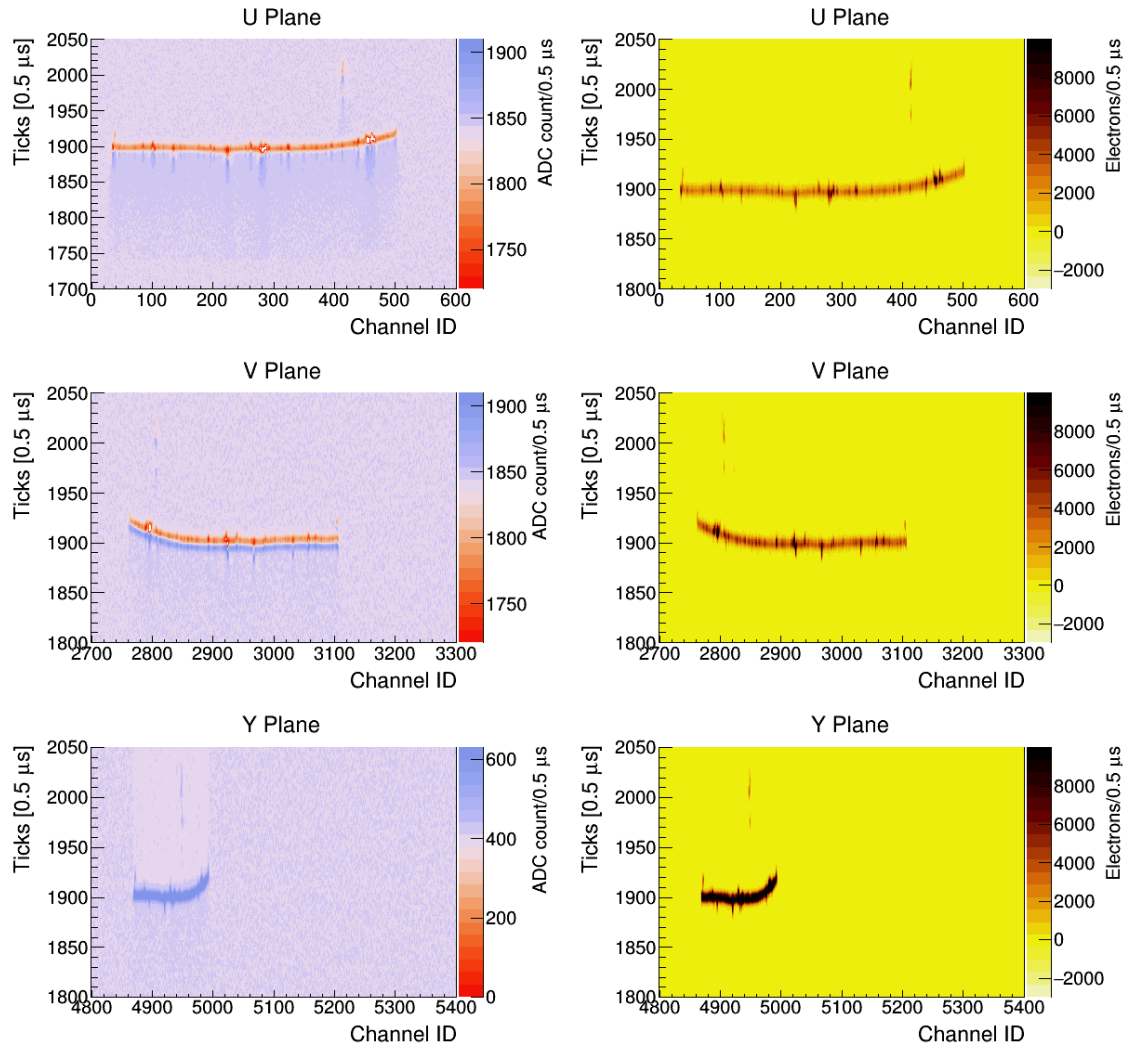
The TPC detector simulation spans detector physics ranging from measures of energy loss by particles traversing the detector to the digitized waveforms produced from a model of the front-end electronics. A data-driven, analytical simulation of the inherent electronics noise is also performed. Figure 22 shows one example event produced by this simulation.

The signal simulation, i.e. the ADC waveform on a given channel,

$$M = (Depo \otimes Drift \otimes Duct + Noise) \otimes Digit, \quad (4.1)$$

is conceptually a convolution of five functions:

*Depo* represents the initial distribution of the ionization electrons created by energy depositions in space and time.



(a) Simulated waveforms.

(b) Extracted charge distributions.

**Figure 22:** Simulated waveforms and reconstructed charge from a nearly isochronous track of a GEANT4-based 5-GeV muon in liquid argon. The X-axis represents the channel (wire) from the three wire planes of MicroBooNE. The Y-axis represents the sampled time ticks (per  $0.5 \mu\text{s}$ ). (a) Simulated waveforms including inherent electronics noise in units of ADC counts. (b) Reconstructed charge in units of  $e^-$  corresponding to the simulated waveforms in (a).

*Drift* represents a function that transforms an initial charge cloud to a distribution of electrons arriving at the wires. Physical processes related to drifting, including attenuation due to impurities, diffusion and possible distortions to the nominal applied electric field, are applied in this function.

*Duct* is a family of functions, each is a convolution  $F \otimes E$  of the field response functions  $F$  associated with the sense wire and the element of drifting charge and the electronics response function  $E$  corresponding to the shaping and amplification of the front end electronics.

*Digit* models the digitization electronics according to a given sampling rate, resolution, and dynamic voltage range and baseline offset resulting in an ADC waveform.

*Noise* simulates the inherent electronics noise by producing a voltage level waveform from a random sampling of a Rayleigh distributed amplitude spectrum and uniformly distributed phase spectrum. The noise spectra used are from measurements with the MicroBooNE detector after software noise filters, which have excess (non-inherent) noise effects removed.

These functions are defined over broad ranges and with fine-grained resolution. The characteristic scales are set by the variability and extent of the field response functions and the sampling rate of the digitizer. Their range is set by the size of the detector, which is related to the length of time over which one exposure is digitized. With sub-millimeter field variability,  $0.5 \mu\text{s}$  sampling, a detector of several meters in extent, and a readout over several milliseconds, the size of each dimension of these functions is  $10^3 - 10^5$ . A naive implementation of the required convolution is not possible with commercial computing hardware. The remainder of this section describes each term in equation 4.1 including the methods employed to reduce the dimensionality.

#### 4.2.1 Initial distribution of charge depositions

The simulation takes as input a distribution of initial charge depositions - free ionization electrons from charged particles traversing the liquid argon medium. In order to reduce the size of the input, the simulation requires charge depositions to be defined as a set of discrete, localized depositions

$$Depo_i = (q_i, t_i, \vec{r}_i), \quad (4.2)$$

where  $q_i$  is the number of ionization electrons at the given point  $(\vec{r}_i, t_i)$  in space and time.

The scale at which charge deposition is localized must be chosen to balance computation time and to ensure that discreteness is smoothed out by subsequent convolution terms. In practice, this limitation is well matched to the form of results produced by tracking simulations such as those based on GEANT4 [35] implemented in LArSoft (Liquid Argon Software) [34].

The user may directly supply  $q_i$  in terms of ionization electrons or in terms of the amount of energy lost by particles over a given step of the tracking simulation (i.e.  $dE/dx$  over distance  $dx$ ). If the latter is provided, the simulation will apply the appropriate Fano factor [36], recombination [37–39] and their associated statistical fluctuations in generating the ionization charge.

#### 4.2.2 Drift transport and physics

The simulation supplies a full set of physical processes related to the transport of ionization electrons through liquid argon under the influence of an applied electric field. These processes include electron attenuation (corresponding to electron attachment on impurities in liquid argon), longitudinal and transverse diffusion [5], and transport. The default transport is performed neglecting distortions due to the build up of space charge [40]. As a result, initial point-like depositions are typically provided as points but they may have characteristic widths  $(\sigma_{\perp}, \sigma_{\parallel})$  in the transverse direction and along the nominal drift, respectively, as a 3D Gaussian cloud

$$Depo_i \otimes Drift \rightarrow Depo_i(q_i, t_i + t_{drift}, \vec{r}_i|_{x=x_{rp}}, \sigma_{i\perp}, \sigma_{i\parallel}), \quad (4.3)$$

where  $\sigma \cong \sqrt{2 \cdot D \cdot t_{drift}}$ ,  $t_{drift}$  is the drift time, and  $D$  is transverse ( $D_T$ ) or longitudinal ( $D_L$ ) diffusion coefficients, respectively [5]. The transport term of the convolution transforms each deposition as in expression 4.3 independently until the center of the resulting distribution of ionization electrons reaches a *response plane*. The response plane is normal to the nominal drift direction which is along the  $x$  coordinate axis and is located near the wire planes. Its location  $x_{rp}$  exactly coincides with the plane containing the starting locations (10 cm) of the drift paths on which the field response functions are defined/simulated.

Diffusion gives the initial deposition a finite extent in the transverse and longitudinal directions. Each deposition is then trifurcated for each wire plane. The transverse location and extent are transformed to measures  $\rho$  along the pitch direction for the given plane. The longitudinal extent is transformed to a time-based measure using the nominal drift speed relative to the time at which the center of the deposition reached the response plane. This trifurcation transforms a single 3+1 space-time dimensional problem into three smaller 1+1 problems. The single remaining space coordinate is the transverse measure along the pitch direction of each wire plane.

### 4.2.3 Detector field and electronics response

The *Duct* term is itself a convolution  $F_j \otimes E$  of the field and electronics responses, respectively. The first function  $F_j$  describes the current induced on a sense wire due to the passage of a nearby unit charge along a path  $j$  starting a distance  $\rho_j$  in the wire pitch direction. Given a wire at  $\rho = 0$ , these paths are shown in figure 2. The field response employed in the simulation is a 2D Garfield calculation, meaning that it is independent of the position along the wire direction for each wire plane. However, this 2D calculation is meant to serve as a good approximation of the realistic 3D field response averaging along the wire direction.

The second function  $E$  includes two parts as shown in figure 6 corresponding to the pre-amplifier and two RC filters. In addition, an intermediate gain of 1.2 is included.  $E$  determines the voltage response of the front-end amplifiers to the instantaneous application of a unit charge as their input. In simulation, the electronics response is taken to be constant for all channels.

The convolution  $F_j \otimes E$  is independent of the distribution of drifted charge and can be calculated separately. Results of such a calculation are shown in figure 4. Instead of performing the convolution through a direct integration in the time domain, a discrete Fourier transform (DFT) is applied on each term, followed by a multiplication in frequency-space and a final inverse DFT. However, in the simulation, subsequent convolution is required in order for the intermediate frequency-space result to be cached for later reuse.

The sampling period is fixed according to the electronics digitization in  $E$ , as the instantaneous current in  $F_j$  must be integrated over each sample. In the discussion below, this convolution of field and electronics responses is referred to generically as a response function.

Given a point charge, the changes of the waveform resulting from the longitudinal Gaussian diffusion and electronics responses (preamplifier, RC filters) are demonstrated in figure 23. Note that the RC filters have an effect on the collection plane's signal, though it is relatively small (less than 1 %). The tail of the RC filter also shows up in the Y plane waveform of figure 22a.

The simulation has the framework to incorporate multiple responses, e.g., different electronics responses corresponding to normal channels or mis-configured channels, as well as different field responses corresponding to shorted wire regions. These specific responses are relevant to real

MicroBooNE data as mentioned in [27] and important in data/MC comparisons as elaborated in [19].

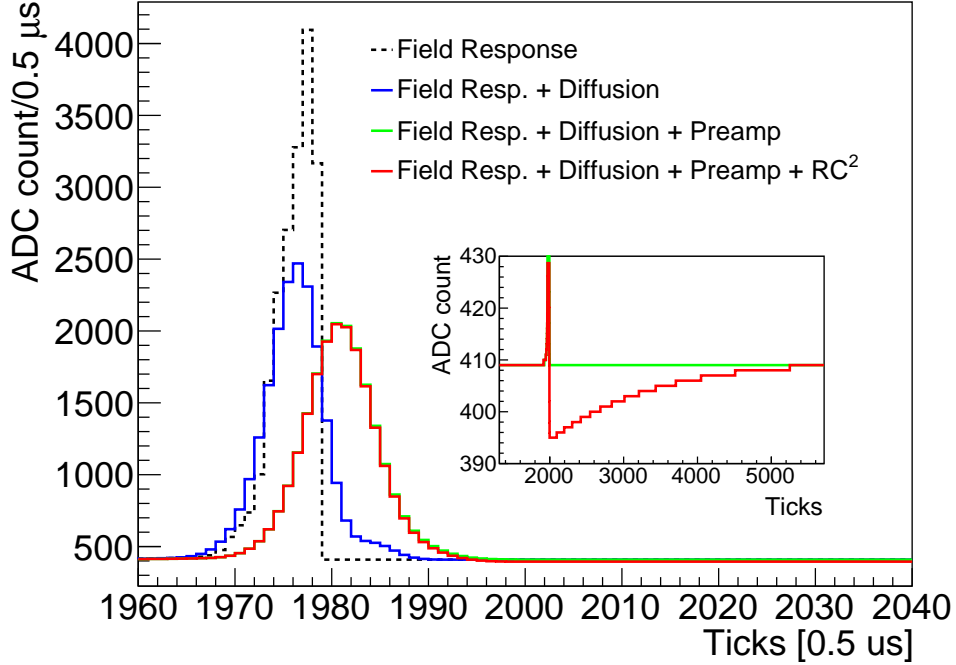


**Figure 23:** Breakdown of a full simulation of a point source of charge. The Y plane waveforms are taken as an example. The ADC baselines for Y plane are set to 409 ADC counts, 200 mV. An inset figure magnifies the long tail from the RC filters. The maximum magnitude of the negative tail is roughly 0.7% of the signal peak. Diffusion is a 2D smearing effect and the plot just shows the result of the central wire.

#### 4.2.4 Performing the convolution

As described above, the drifted charge distribution and response functions now cover a discrete two dimensional domain, where  $\rho_j$  is a measure in the pitch direction relative to a given wire. That is,  $j$  spans the number of nearby drift paths. The simulation has drift paths which cover the central wire region and ten wire regions to either side with ten paths per region. This gives a total of 210 paths per plane centered on each wire of interest.

This span in  $\rho$  is used to identify all depositions that have any portion of their total extent contained therein. It is worth remembering that these depositions are in a parameterized form following a 2D Gaussian distribution. These distributions must be discretized in order to be convolved with the corresponding discrete response function.

There are two aspects to this discretization which are important to its performance and correctness. The first is due to the response functions covering more transverse span than just a single wire region. All depositions falling in the nominal 21 wire regions must be discretized for each wire. Most of these same depositions will also contribute to the neighboring wires. Rediscretizing

for each wire would entail a factor of 20 redundant calculations. Discretizing the entire domain would require a prohibitive amount of computer memory. To overcome computing limitations, the wires of a plane are processed in order of their pitch location starting from the smallest  $\rho$ . As the calculation advances to the next wire, it frees the memory associated with the wire region of the lowest  $\rho$  and discretizes one new wire region at the high end.

The second aspect relates to correctness. The coverage of  $\rho$  by the response functions is very finely grained. Neighboring drift paths are separated by 0.3 mm (1/10 of the wire pitch in MicroBooNE). At this scale, the path-to-path response variation is typically small, within 10%. However, particularly for the induction planes, at any scale of such coverage of  $\rho$  there is an aliasing effect that will occur for elongated charge distributions which fall in a line close to perpendicular to the wire planes. As shown in figure 24, this effect is in a small but non-negligible phase space that must be mitigated. An interpolation is performed using the two nearest response functions at both  $\rho_i$  and  $\rho_{i+1}$ .

In order to calculate the interpolated response, for any wire plane using its own Cartesian coordinate, the deposited charge after drifting can be expressed as  $q(t, z)$ . This charge is to be convolved with the field response  $F(t, x, y, z)$  of which  $x$  is fixed at the starting location of the virtual response plane and  $y$  equivalently averages out. Consider  $\rho_j < z < \rho_{j+1}$  and the two field responses  $F_1(t) = F_j(t, \rho_j)$  and  $F_2(t) = F_{j+1}(t, \rho_{j+1})$ , the convolution is performed as follows:

$$\int_{\rho_j}^{\rho_{j+1}} \{q(t, z) \otimes (F_1(t) \cdot u(z) + F_2(t) \cdot (1 - u(z)))\} dz, \quad (4.4)$$

where  $u(z)$  is the weighting function for interpolation between two calculated paths of field response. Since transverse and longitudinal diffusion are independent processes,  $q(t, z)$  can be re-phased as  $q(t) \cdot Gaus(z)$ . The width and center of the function  $Gaus$  depend on the initial deposition location of the charge. Therefore, expression 4.4 can be simplified as an integral of  $z$  and convolution of  $t$ ,

$$\int_{\rho_j}^{\rho_{j+1}} \{Gaus(z)u(z)\} dz \cdot q(t) \otimes F_1(t) + \int_{\rho_j}^{\rho_{j+1}} \{Gaus(z)(1 - u(z))\} dz \cdot q(t) \otimes F_2(t) \quad (4.5)$$

In practice, any charge deposition at  $z$  between path  $j$  and  $j + 1$  is redistributed to the two positions  $\rho_j, \rho_{j+1}$  against the weight  $\int_{\rho_j}^{\rho_{j+1}} \{Gaus(z)u(z)\} dz$ . The weighting function  $u(z)$  has two options at present,

$$\text{Average : } u(z) = 0.5, \text{ or} \quad (4.6)$$

$$\text{Linear : } u(z) = \frac{z - \rho_j}{\rho_{j+1} - \rho_j}. \quad (4.7)$$

The weight integral can be analytically derived using a Gaussian function and the error function. Linear interpolation more closely reflects the underlying physics as illustrated in figure 24 because linear interpolation lends to a continuous variation of the field response and smooth waveforms at the paths of each calculated field response.

Following *Duct*, a final digitization step is applied, currently supplying a simple ADC model. It is parameterized by the ADC resolution, full scale voltage range and baselines to apply to the input voltage waveforms. For MicroBooNE, a 2-MHz, 12-bit ADC is used with the dynamic voltage range up to 2000 mV.



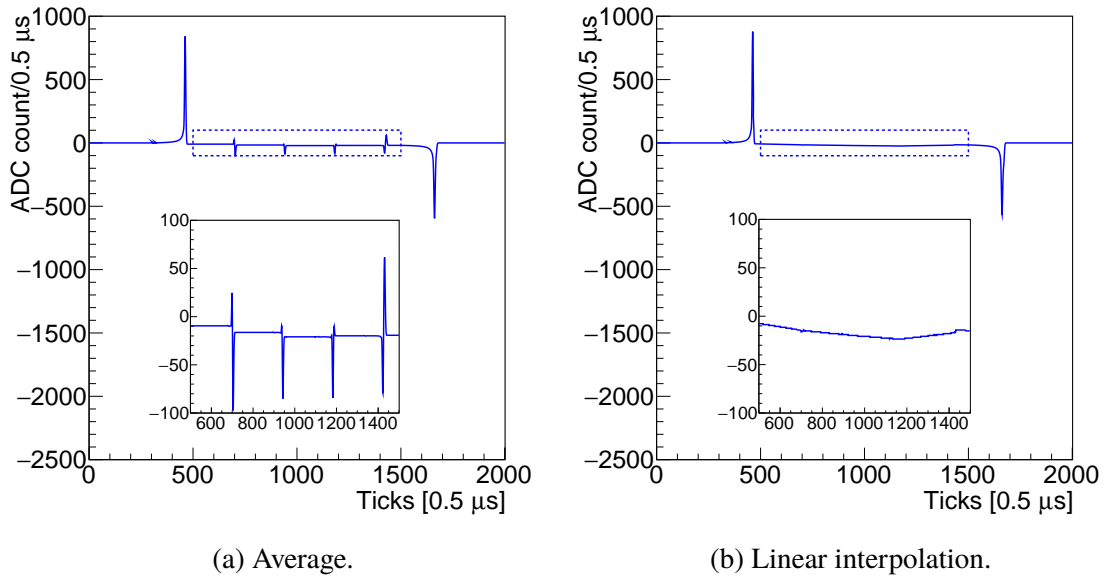


**Figure 24:** Simulated baseline-subtracted waveforms of an induction plane large angle track, near perpendicular to the wire plane. The track covers 6 paths / 5 sub-pitches within a wire region. The inset figure magnifies the waveform in the dashed box, displaying the fine grained field response as well as the cancellation of the bipolar field response at the paths of each calculated field response (boundaries of sub-wire regions). (a) Average weighting, leading to improper cancellation of the bipolar response. (b) Linear interpolation, leading to proper cancellation of the bipolar response.

#### 4.2.5 Truth values

A new set of input quantities of the simulation (MC truth) is constructed to compare the ionization electrons generated by Geant4 and propagated to the wire planes to those reconstructed after signal processing. MC truth retains track ID and PDG code (particle species) information (from the generator) to facilitate the assessment of the efficacy of downstream reconstruction algorithms. As described in section 3.2.2, software filters are applied in signal processing to extract the ionization signal and mitigate high frequency noise. These filters smear the charge signal in the time and wire dimensions, or longitudinally and transversely, respectively. For equitable treatment of MC truth to that posed by signal processing, the same high frequency time and wire software filters are treated directly to the ionization electrons as a function of time and wire in construction of the MC truth signal.

#### 4.2.6 Noise simulation

The signal simulation described above produces ADC-level, time-domain waveforms in each channel. To simulate detector data, waveforms arising from inherent electronics noise are added to the signal waveform. An analytic method to simulate the noise is introduced below and it is applicable to a wide range of noise simulations other than the inherent electronics noise.

This method was motivated by [41]. The core of this method is to simulate the stochastic behavior of the noise in the frequency domain. The stochastic effect originates from the random occurrence of each noise pulse (e.g. due to thermal fluctuation) and the method is applicable in

the condition that the occurrence of each noise pulse is uniformly distributed in time. With this condition, the noise stochastic behavior in the frequency domain follows a random walk process and the analytic mathematical description of the random walk can be used to model the noise. A single parameter - the mean frequency amplitude - is required for the noise simulation for each frequency. This parameter is extracted from data. Details of the method are described below.

In general, the inherent electronics noise can be categorized into several types: white noise, flicker noise (pink noise), and Brownian noise (red noise) [42–44]. The corresponding power spectrum densities are constant, proportional to  $1/f$ , and proportional to  $1/f^2$ , respectively. The total noise divergence (at infinite frequency for white noise and at infinitesimal frequency for the latter two types of noise) does not occur because the detector devices themselves have cutoffs at low and high frequencies. Meanwhile, the power spectrum can be altered by the response of the dedicated electronics device.

Given any kind of inherent electronics noise pulse, assume its function in the time domain is  $i(t)$  and in the frequency domain is  $I(\omega)$ . For white noise  $I(\omega)$  is  $G(\omega) \cdot 1$  and for flicker noise  $G(\omega) \cdot \frac{1}{\sqrt{\omega}}$ , where  $G(\omega)$  includes the normalization for a single noise pulse as well as the response of the electronics device.

Consider a train of noise pulses: the function in time domain is

$$f(t) = \sum_{n=1}^N q_n \cdot i(t - t_n), \quad (4.8)$$

and in frequency domain is

$$F(\omega) = \sum_{n=1}^N q_n \cdot I(\omega) \cdot e^{-j\omega t_n}, \quad (4.9)$$

where  $q_n$  is the sign (+ or -) of the noise pulse,  $n$  is the index,  $j$  is the imaginary unit, and  $t_n$  is the occurrence time of each noise pulse, uniformly distributed in time.

Absorbing  $q_n$  and the phase of  $I(\omega)$  into the phase term, equation 4.9 can be rewritten as

$$F(\omega) = \sum_{n=1}^N |I(\omega)| \cdot e^{-j\theta_n(\omega)}, \quad (4.10)$$

where  $\theta_n(\omega)$  is uniformly distributed in  $[0, 2\pi)$  if<sup>5</sup>  $\omega \cdot t_N \gg 2\pi$ .

In the 2D complex plane, given a frequency  $\omega$ , equation 4.10 follows a 2-dimensional random walk with the angle  $\theta_n$  uniformly distributed over  $[0, 2\pi)$ . Since the number of steps,  $N$ , is large enough, the probability density distribution of the distance ( $r$ ) from the origin to the end point can be analytically described by [45]

$$R(r; \sigma) = \frac{r}{\sigma^2} e^{-\frac{r^2}{2\sigma^2}}, \quad (4.11)$$

where  $R(r; \sigma)$  is the Rayleigh distribution with the mean value of  $\sigma \cdot \sqrt{\pi/2}$  and  $\sigma^2 = 0.5 \cdot N \cdot |I(\omega)|^2$ .

Then, we can represent equation 4.10 in a polar form by

$$F(\omega) = r(\omega) \cdot e^{-i\alpha\omega}, \quad (4.12)$$

---

<sup>5</sup>In practice, the discrete Fourier transform naturally discards the information if  $\omega \cdot t_N < 2\pi$  and the analysis technique, e.g. region of interest (ROI), can further suppress the low frequency noise. The improper simulation of low frequency noise which does not meet the condition  $\omega \cdot t_N \gg 2\pi$  can be ignored.

where  $r(\omega)$  follows the Rayleigh distribution and  $\alpha_\omega$  is uniformly distributed in  $[0, 2\pi)$ . If  $N$  is large enough, the  $\alpha_\omega$ 's are mutually independent for different frequencies.

Equation 4.11 is equivalent to two independent Gaussian distributions on the real and imaginary axes with the same standard deviation  $\sigma$ , which is the only parameter in the corresponding Rayleigh distribution. This feature can be employed to simulate the random walk (noise) and to deduce that the summation of multiple different step length random walks can be described as in equation 4.12, because of the additive property of Gaussian distribution.

As a result, all sources of noise can be summed, and for each frequency the simulation can be done by sampling the Rayleigh distribution, which has a single parameter  $\sigma_{total}$  to randomize the frequency amplitude with a uniformly distributed phase from 0 to  $2\pi$ . The  $\sigma_{total}(\omega)$ , i.e. the mean frequency amplitude divided by  $\sqrt{\pi/2}$ , can be extracted from the data. In this paper, the mean frequency amplitude was extracted from MicroBooNE data as shown in figure 25. An inverse Fourier transformation of the randomized noise frequency spectrum will provide the final noise waveform in the time domain.

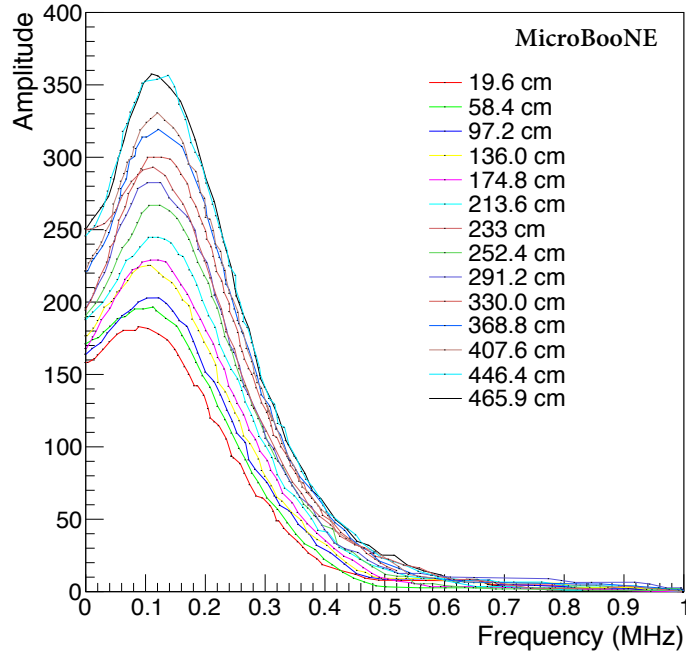


**Figure 25:** Mean frequency amplitude of the inherent electronics noise for different lengths of wires are deduced from MicroBooNE data using ADC waveforms after noise filtering and mis-configured channel corrections [27]. A small constant term which is not associated with the pre-amplifier is subtracted. The length of 233 cm is associated with collection plane wires, and the rest are associated with induction plane wires. The mean amplitude for intermediate wire lengths is obtained by interpolation.

### 4.3 Quantitative evaluation of the signal processing

A qualitative demonstration of the signal processing performance is shown in figure 22. Several features of the raw and reconstructed tracks can be seen: the fine structure of the charge depositions

along the track, the short tracks off the main trajectory, and the high charge density of the track in the collection plane, mainly due to the small angle of the track with respect to the Y wires.

In this section, we present a quantitative evaluation of the signal processing. This evaluation addresses the intrinsic charge smearing in the time and wire dimensions, charge matching among the three wire planes, and reconstructed charge resolution, bias, and inefficiency for large angle tracks. Understanding these effects is critical for subsequent event reconstruction. Below are the definitions of these quantities.

*Charge* – the number of ionization electrons. For a track (line charge), a constant charge density is used.

*Time smearing* – the standard deviation of the Gaussian distribution of the deconvolved charge time spectrum on a wire, specifically associated with a point source of charge.

*Wire smearing* – the fraction of the integrated deconvolved charge on a wire with respect to the total deconvolved charge over the entire range of fired wires, specifically associated with a point source of charge.

*Charge bias* – the mean fractional difference between the total deconvolved charge and the true charge. In terms of a track (line charge), the mean value of the distribution of each wire's integrated deconvolved charges from a range of wires will be used to calculate the charge bias with respect to the true charge within one wire pitch.

*Charge resolution* – the standard deviation of the total deconvolved charge relative to the mean deconvolved charge. In analogy to the definition of charge bias, in terms of a track (line charge), the distribution of each wire's integrated deconvolved charges from a range of wires will apply.

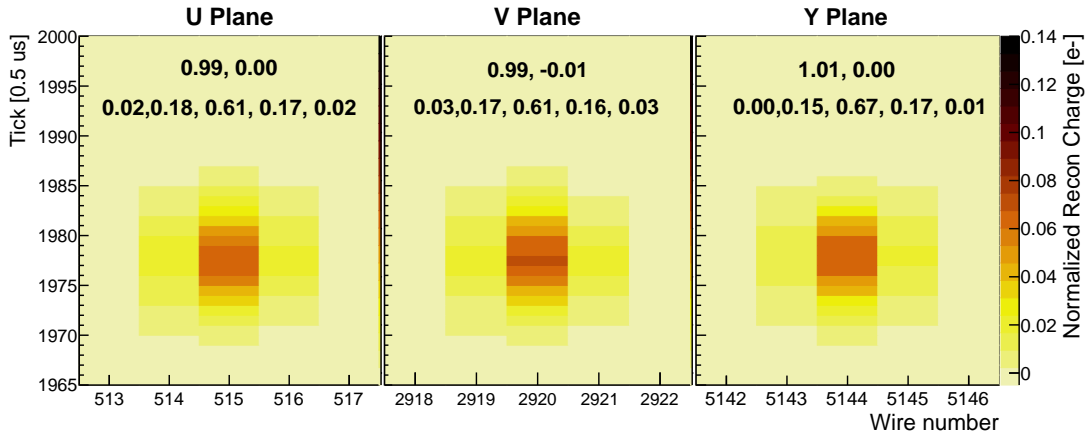
*Charge inefficiency* – specifically associated with tracks (line charges), the fraction of the wires which have ZERO deconvolved charge (no ROI found). Note that these wires will not be involved in the calculation of charge bias or charge resolution.

#### 4.3.1 Basic performance of the signal processing

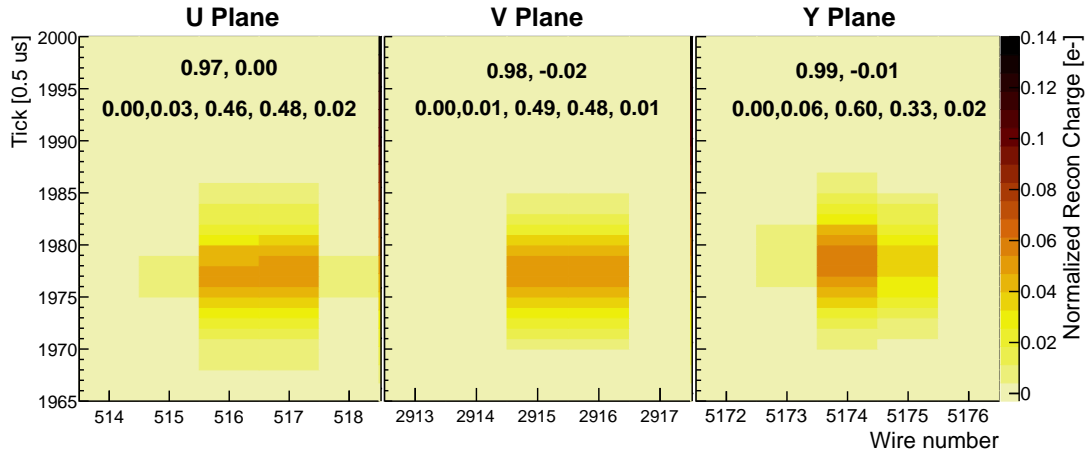
The deconvolved results in the three planes for a point source of charge are shown in figure 26. Ten thousand electrons were simulated one meter from the wire planes. No noise was included; only diffusion and response functions were simulated. The electronics responses in simulation and deconvolution are identical. The results for two extreme positions of the point source of charge were presented, at the wire and at the wire region boundary, respectively.

**Time smearing** is about 2.7 ticks and 2.3 ticks for induction and collection planes, respectively, largely dictated by the high frequency software filters in the signal processing. A one meter drift span provides a longitudinal/time smearing of about 2 ticks.

**Wire smearing** is indicated by the numbers in the second row in figure 26. More than 60 % of charge is extracted by the closest wire if the point source of charge is close to the wire. For the induction plane, about 50% of the charge is extracted by both the closest wire and the adjacent wire if the point source of charge is close to the boundary of the wire region, due to the long range of



(a) Point source at the wire (0.0 mm transverse position relative to the closest wire).



(b) Point source at the wire region boundary (1.5 mm transverse position relative to the closest wire).

**Figure 26:** Point source charge after signal processing. Charge is shared across wires on a given plane. The fractional charge recovery relative to  $1 \times 10^4$  electrons is indicated by the numbers in the top row, negative charge by the former number and the positive charge by the latter one, rounded to 0.01. Relative charge per wire is indicated in the lower row.

induction as shown in figure 2. For the collection plane, this effect is smaller due to the predominant collection signal on the closest wire.

**Charge bias** is at the 1% level. In this case, it originates from the mismatch of the field response in signal simulation (fine-grained) and deconvolution (average response). Positive charge (a fraction of distorted deconvolved charge spectrum below zero) can also be reconstructed due to this mismatch. A 1-m drifting diffusion is applied which smears the charge deposition and reduces the mismatch of the average response and position-dependent response within one wire pitch. As a result, the extracted charge across the three wire planes is reasonably well-matched. Charge bias arising from small position-dependency within the wire region is inevitable.

The deconvolved charge spectrum of any event topology can be obtained through a convolution with the point-charge “response”, i.e. the deconvolved charge spectrum of point-charge as shown in figure 26. For instance, it is anticipated that the charge bias should also be at the 1% level for a track of charge. However, including the electronics noise has a significant impact on the performance, as explained in the following section.

#### 4.3.2 Charge resolution due to electronics noise

Given an energy deposition, the overall charge resolution originates from the fluctuation of the number of ionization electrons in the signal formation. Several effects are considered, including the statistical fluctuation in the production of ionization electrons, recombination with argon ions, and absorption in drifting due to impurities of liquid argon. The total statistical fluctuation can be ignored relative to the impact of electronics noise. For instance, a MIP track corresponds to  $\sim 10^4$  ionization electrons within one wire pitch. The statistical fluctuation in production is  $\sqrt{10^4 \cdot 0.1} = 32$  and in drifting is  $\sqrt{10^4 \cdot 0.7 \cdot (1 - 0.7)} = 50$ , where 0.1 is the typical Fano factor [36] and 0.7 is the typical survival probability of ionization electrons considering recombination and absorption [37–39]. By contrast, the equivalent noise charge (ENC) after deconvolution is  $\sim 1\text{k}$  electrons.

Thus, the electronics noise is the main contributor to the charge resolution. Before deconvolution, the ENC is roughly the same for all three wire planes (about  $300 \pm 50$  electrons irrespective of wire length) as shown in [27] and illustrated in figure 25. After deconvolution, the noise-induced charge is magnified from the ENC value, especially by the bipolar field response of the induction planes. When performing the deconvolution in the frequency domain for the induction planes, the induction plane bipolar response is in the denominator. This response is suppressed at low frequencies (see figure 12), thus amplifying the low frequency noise. Figure 27 presents the noise-induced charge after signal processing for the full waveform. For the induction plane, there is a very large contribution from the lowest frequencies. By contrast, the collection plane has a similar deconvolved charge distribution as the original noise waveform, apart from a unit conversion from electrons to ADC counts ( $\sim 182 e^-/\text{ADC}$ ).

ROI finding aims to identify a ROI window based on the ‘true’ signal; therefore, the charge resolution due to noise can be obtained by analysis of various ROI windows. Two types of charge resolution will be studied here. The first type is the total charge resolution within the entire ROI window, which is related to the energy reconstruction for each wire, i.e.  $dE/dx$ . The second type is the single bin charge resolution, where one bin corresponds to the minimum time unit for the subsequent event reconstruction (e.g. 1 bin may account for multiple time ticks). Figure 28 illustrates the total charge resolution and bin charge resolution for each wire plane as a function of ROI window length.

A linear baseline subtraction is needed for the induction planes to remove the distortion introduced from the large amount of low frequency components as discussed in section 3.2. For the collection plane, this linear baseline subtraction is unnecessary. In fact, if the baseline subtraction were performed, it would contribute to additional smearing. The underlying mathematics is implied by the charge spectrum in the frequency domain as shown in figure 27. The induction plane has many more low frequency components and stronger bin-to-bin correlations, whereas the collection plane has smaller bin-to-bin correlations.

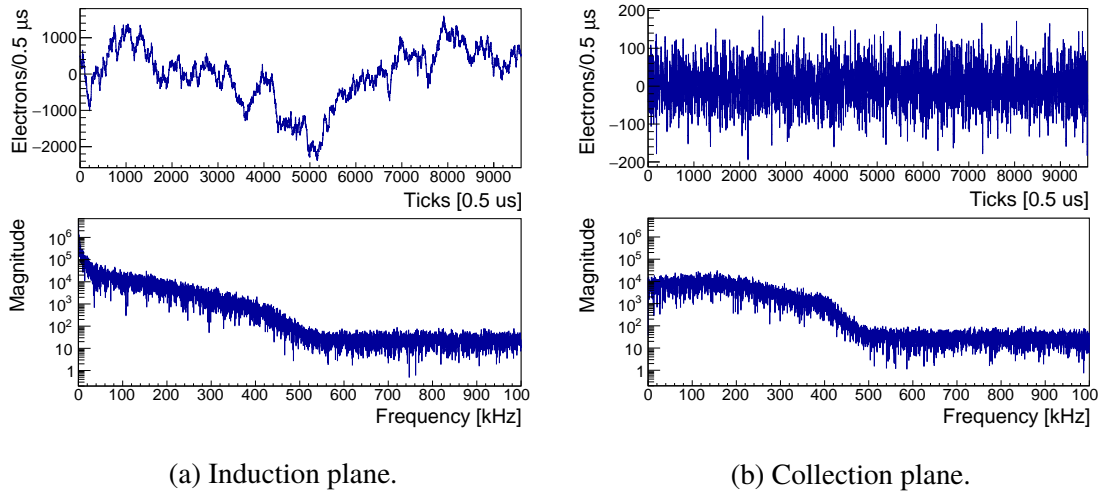


**Figure 27:** Noise-induced charge distribution after signal processing for the full waveform. The top row is in the time domain. The bottom row is in the frequency domain after FFT.

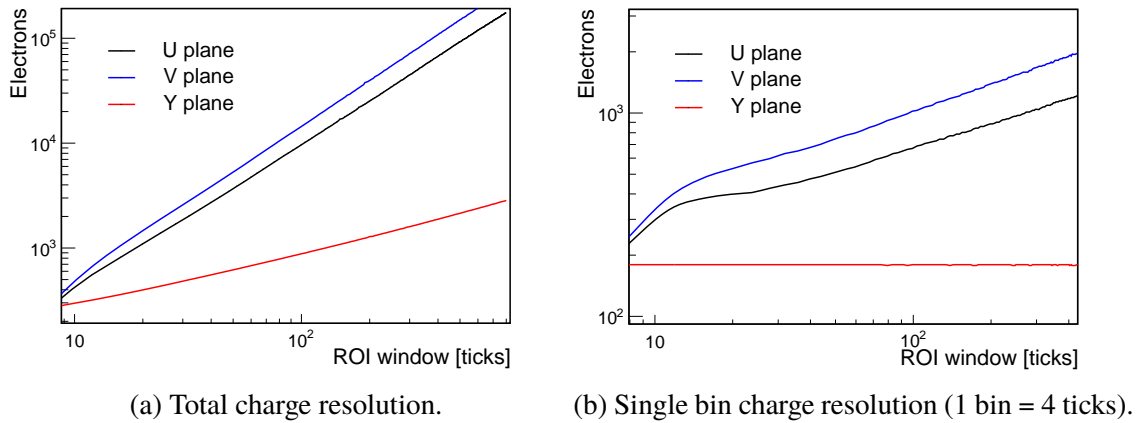


**Figure 28:** Charge resolution (in units of electrons) due to the electronics noise. 1 tick = 0.5  $\mu$ s. (a) Total charge resolution within the entire ROI window. (b) Single bin charge resolution within the minimum time unit for subsequent event reconstruction. See text for additional explanation of the variation of the single bin charge resolution for the induction plane.

The single bin charge resolution is constant for the collection plane. For the induction plane, the single bin charge resolution increases since the impact of the baseline correction decreases with an increase of ROI window length. In addition, the single bin charge resolution for the induction plane depends on the location of the bin within the ROI window. The bin resolution at the boundaries of the ROI window is zero and increases rapidly for the intermediate region like a step function. The “flat top” of the step has a shallow valley at the center of the ROI window which varies in flatness up to 20%. For bins ranging from 1 to 6 ticks, the single bin charge resolution is roughly proportional to the number of time ticks in one bin.

Based on figure 28, given the signal length, the ROI window should be as small as possible

while covering the signal in order to improve the resolution. In general, for a point source of charge or a line charge close to parallel to the wire plane (small  $\theta_{xz}$ ), the ROI length is typically  $\sim 20$  ticks, driven by the time smearing.

Due to the charge smearing, the ability to identify the ROI boundaries is impacted by a low signal-to-noise ratio locally. The variation of the ROI window length in turn alters the charge bias (see section 4.3.3) and noise-induced charge (leading term in charge resolution as shown in figure 28), introducing an additional smearing of the total deconvolved charge as part of the charge resolution. This additional smearing comprises up to 10 % of the total charge resolution.

### 4.3.3 Charge bias due to thresholding in ROI finding

Waveform ROI finding is required due to noise, especially that magnified by deconvolution in the induction planes. As a consequence, a threshold (see section 3.2.3) based on RMS noise on the signal strength dictates the ROI window size on the charge spectrum. The “true” charge is smeared after signal processing and a fraction of deconvolved charge falls below the ROI threshold. Though extension of the original ROI window is performed, signal loss can occur due to its exclusion from the final ROI window. This is the major source of charge bias given that the use of the average field response in signal processing has limited impact (see section 4.3.1). For instance, if noise is included, the deconvolved charge in the distant adjacent wires in figure 26, i.e. a few percent of the total charge shared by the  $\pm 2$  wires, will be overwhelmed by noise and entirely below the ROI threshold; thus, the charge is left absent from the signal processing. Additional results in the context of line charges can be seen in figure 30.

### 4.3.4 Inefficiency of line charge extraction

Because of the charge bias and charge resolution, signal processing can be inefficient for specific event topologies, which means the deconvolved charge spectrum is entirely below the ROI threshold and no ROI window is created. This effect is especially pronounced in the induction planes for prolonged tracks with large  $\theta_{xz}$ , where the bipolar response causes a suppression of the signal, while at the same time increasing the noise.

The hits on a track tend to share the same  $\theta_{xz}$ , and this can lead to gaps in the identified track or even the complete disappearance of the reconstructed track. Disconnected or absent tracks pose a challenge for pattern recognition with regard to the track reconstruction as well as vertex identification.

### 4.3.5 Performance of line charge extraction

To evaluate the signal processing performance of the line charge extraction, various topologies were simulated. As described in section 2.3, the nominal coordinate system is the detector (collection plane’s) Cartesian coordinate system, with the  $y$ -axis in the vertical up direction, the  $y$ -axis in the drifting field direction, and the  $z$ -axis in the beam direction. The line charge is located on this  $x - z$  plane with  $\theta_y = 90^\circ$  and a set of varying  $\theta_{xz}$ ’s which define the shape of the signal. The simulated charge density is  $1.6 \times 10^4$  electrons per 3 mm (wire pitch) along the trajectory from a 1-meter MIP track centered one meter from the wire plane. Diffusion and inherent electronics noise are applied in the simulation.



Here one line charge corresponds to two  $\theta_{xz}$  angles, as in  $\theta_{x'z'}$  and  $\theta_{xz}$  for the induction planes (same value for U, V planes) and collection plane, respectively. In figure 29,  $\overline{OA}$  and  $\overline{OA'}$  are the projections of the track on wire pitch direction for collection plane and induction plane, respectively. In this case ( $\theta_y = 90^\circ$ ), because  $\overline{OA} = 2 \cdot \overline{OA'}$  as a result of the  $60^\circ$  rotation of induction wires,  $\tan\theta_{x'z'} = 2 \cdot \tan\theta_{xz}$  and the total deposited charge within one wire pitch which is inversely proportional to the length of projection on wire pitch direction is scaled up by a factor of two for the induction planes.

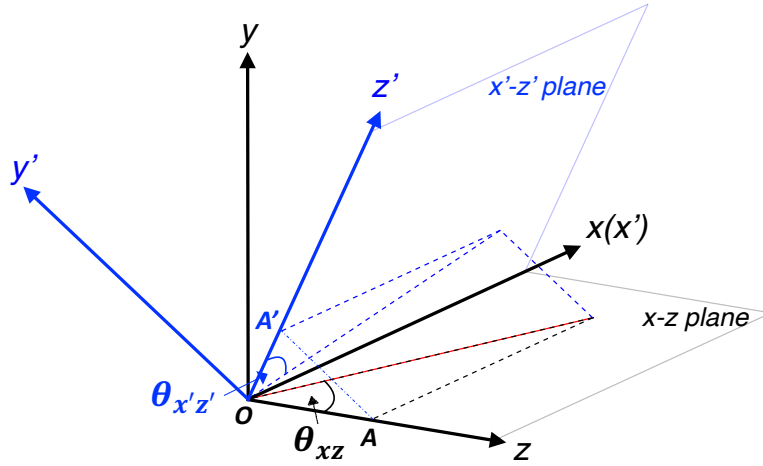


**Figure 29:** Illustration of the line charge employed to evaluate the signal processing performance. Coordinates and angles are defined in figure 8. The line charge (red line) is located on the  $x - z$  plane (collection plane coordinate, black axes). The corresponding projection on the  $x' - z'$  plane (induction plane coordinate, blue axes), which is a  $60^\circ$  rotation of the  $y(z)$ -axis around  $x$ -axis, is plotted as well. Projections on either wire pitch direction ( $\overline{OA}$  and  $\overline{OA'}$ ) are also indicated and  $\overline{OA} = 2 \cdot \overline{OA'}$ .

In general, the performance of the line charge extraction deteriorates with increasing  $\theta_{xz}$  as shown in figure 30, where  $0^\circ$  corresponds to a track parallel to the wire plane (isochronous) and  $90^\circ$  to a track perpendicular to the wire plane. The shape of the reconstructed charge spectrum as shown in figure 31 is dominated by the Gaussian smearing for small  $\theta_{xz}$ , or by the track topology for large  $\theta_{xz}$  in which case the contributions from the charge in neighboring wires are stretched in time and produce a triangular-like shape. A larger  $\theta_{xz}$  corresponds to a wider (larger ROI window) and flatter (smaller signal-to-noise ratio) reconstructed charge distribution, therefore associated with a larger charge resolution and bias.

As explained in section 4.3.4, due to the bipolar response cancellation (see figure 9) and magnified noise (see figure 27), the induction plane has considerably worse performance than the collection plane and is more sensitive to large  $\theta_{xz}$ . Specifically, the induction plane has a significant inefficiency of charge extraction for large  $\theta_{xz}$ . This inefficiency is related to diffusion which introduces an additional smearing. In figure 30, the result corresponds to the average performance considering diffusion along the track.

The extreme case of a long perpendicular track ( $\theta_{xz} = 90^\circ$ ) is not shown in figure 30. For

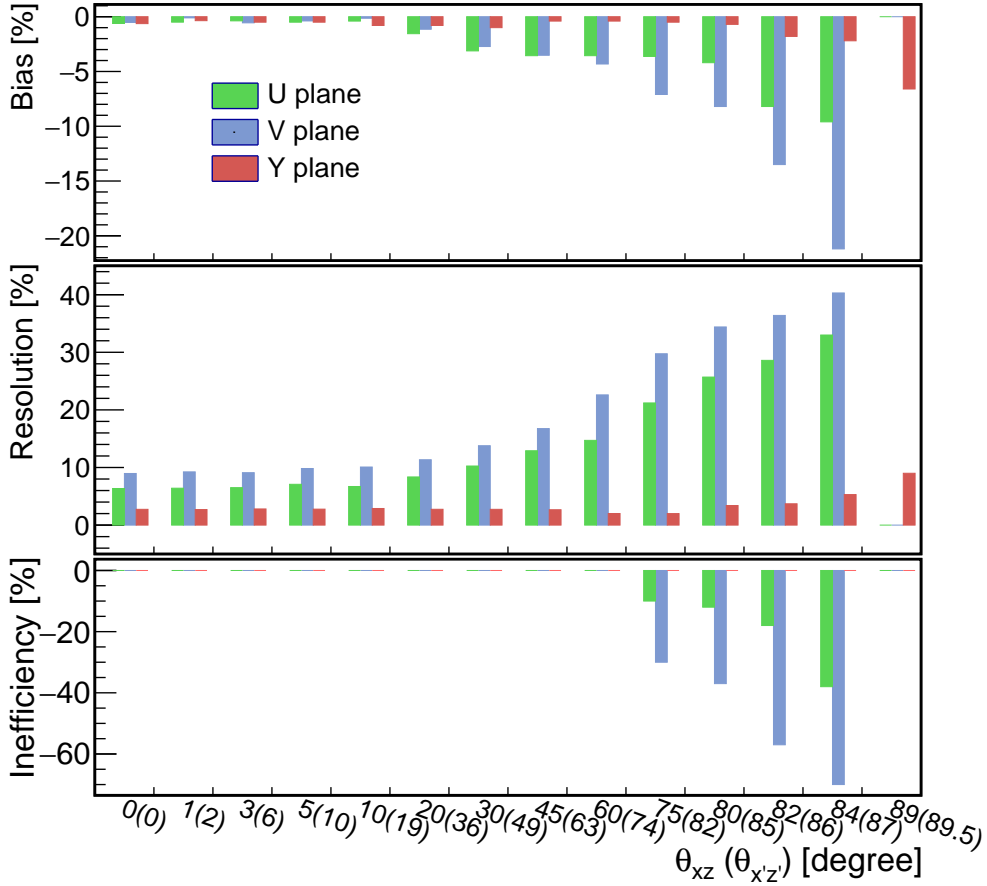


**Figure 30:** Charge bias, resolution, and inefficiency of the reconstructed charge in one wire pitch as a function of  $\theta_{xz}$  ( $\theta_{x'z'}$ ). The line charge is simulated assuming a 1-meter MIP track. Any wire/channel with no charge reconstructed is included in the inefficiency calculation and ignored in the resolution and bias calculations. The last bin ( $89.5^\circ$ ) for induction plane corresponds to full inefficiency of charge extraction and has no input for the resolution and bias calculations. The Y-axis is relative to the ‘true’ charge deposition within one wire pitch before drifting.

the induction planes, similar to the last point in this figure, a long perpendicular track has zero efficiency to extract charge, with the exception of the ends of the track which have non-zero efficiency. However, for physics analyses, the phase space around this extreme case, e.g.  $89^\circ$ - $90^\circ$ , can be ignored, because, in practice, multiple scattering of the particle along a trajectory most likely results in a few degree path deflection. Moreover, for a high energy neutrino beam experiment with the predominance of forward-going event topologies, this impacted phase space is even smaller. For the collection plane, there is still a high efficiency to reconstruct the charge if the track is perpendicular to the wire plane<sup>6</sup>. Similar to a point source as shown in figure 26, the reconstructed charge is shared by adjacent wires.

<sup>6</sup>If the track is prolonged in time, the waveform may be identified as noise baseline shifting and filtered.

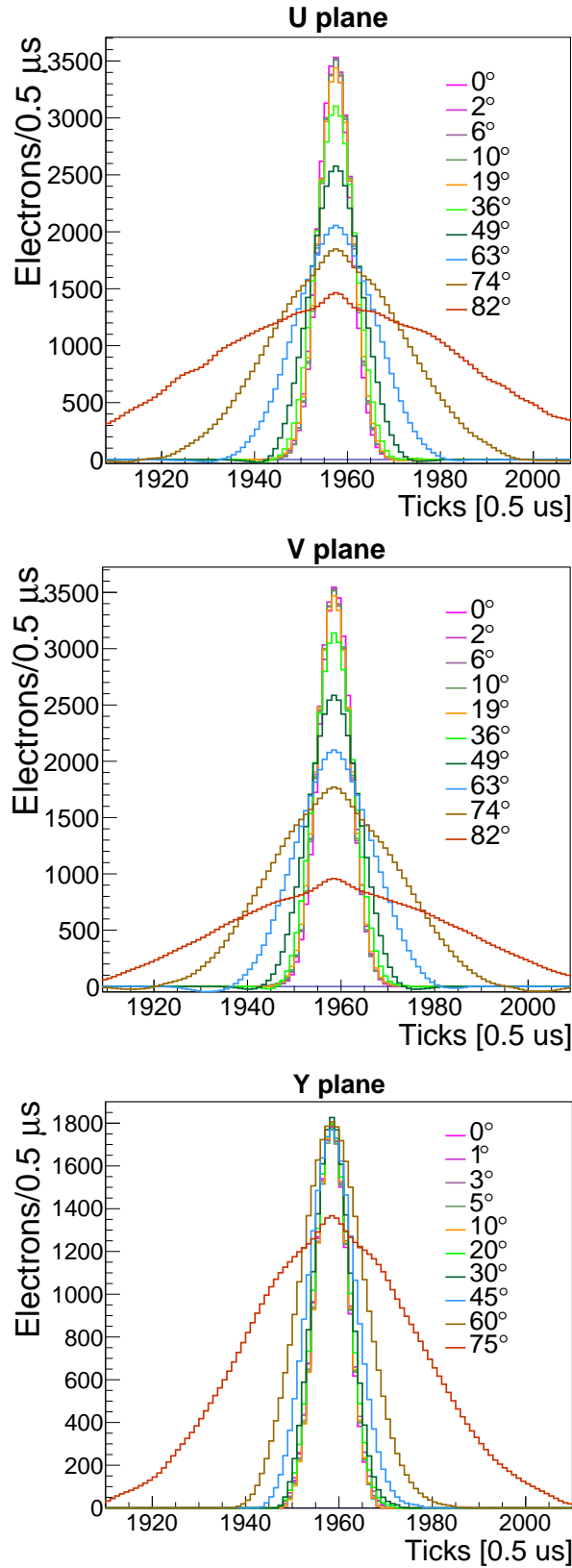


**Figure 31:** Average reconstructed charge distribution within one wire region for the three wire planes at various  $\theta_{xz}$  values corresponding to figure 30.

## 5 Discussion

The signal processing and TPC simulation described and evaluated here allows for a detailed appraisal of cosmic and neutrino-induced TPC event reconstruction in MicroBooNE. For example, with this work, the study of cosmic ray reconstruction efficiencies in MicroBooNE, as shown in [46], can be extended to address the reconstruction efficacy of tagged cosmic events at the raw waveform level in MicroBooNE. However, the current state of signal processing and TPC simulation is not without deficiencies even though we have ideal implementations of the TPC and electronics designs. Some of these shortcomings and methods to remedy them are discussed in the following section.

### 5.1 Limitations of 2D field responses

As described above, this work relies on calculating field response functions using a simplified 2D model of the MicroBooNE detector. While these calculations are an improvement over previous ones in terms of including both fine-grained variations and more correct long-range induction, there exists some uncertainty and concern about any residual limitations. This section lists the potential limitations, discusses some remediation and enumerates the technical challenges to overcome.

The current model assumes three parallel wire planes which extend to infinity in both transverse directions and are limited transversely to ten wires on either side of the central wire of interest. As such, the model cannot accommodate detector edges nor variations in individual wire location, angle, or bias voltage. The 2D nature disallows accounting for any possible variation along the direction of the wires and in particular requires a somewhat arbitrary choice to be made for the transverse location of wires in one plane relative to the others.

Also as described above, the induced current is appreciable over a greater range than just the wire region nearest to a given element of drifting charge. At the same time, after the distance of ten wire regions, the strength is reduced to a negligible level in most cases. This means that multiple sets of 2D field response functions can be used to model variations on a patchwork basis. Such an approach is developed for modeling the MicroBooNE wires with bias voltages consistent with a short to ground. This improvement still suffers from the above limitations, and in particular must have the parameters governing bias voltage and relative wire positions tuned to match real data from the detector.

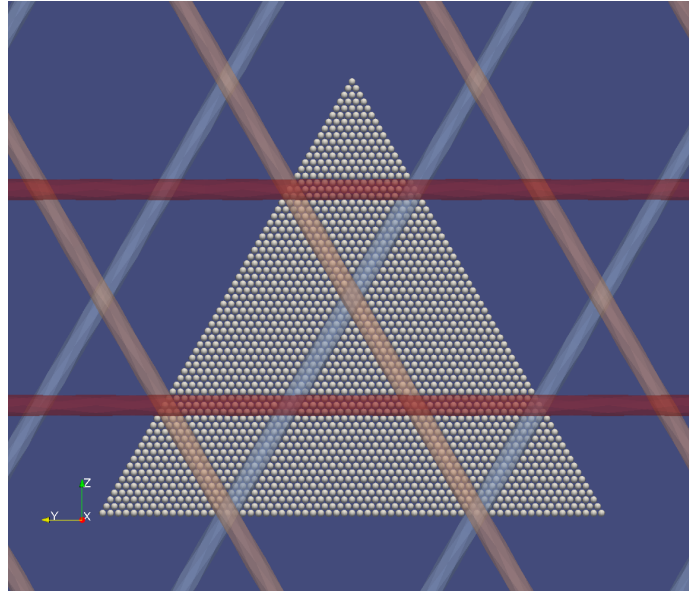
One approach to address these limitations is to develop a new model which spans all three spatial dimensions. This approach goes beyond what the current Garfield 2D analytic calculation provides.

The Finite Element Method can be applied to 3D geometry of arbitrary construction. The required computation time for this method naively scales as the volume of the geometry relative to the feature size. Calculations spanning tens of centimeters with wires of 0.15 mm diameter become computationally challenging. This feature can be somewhat mitigated by applying adaptive grid techniques. Development of FEM based 3D field calculations is an active area of investigation but currently they only span a subset of the total required volume.

Another promising approach to calculate the electrostatic fields in 3D is to use the Boundary Element Method [47]. Its computation cost scales as the surface area instead of the volume of the geometry. An initial pursuit of this approach has been investigated [48] and some examples of its results are included below.

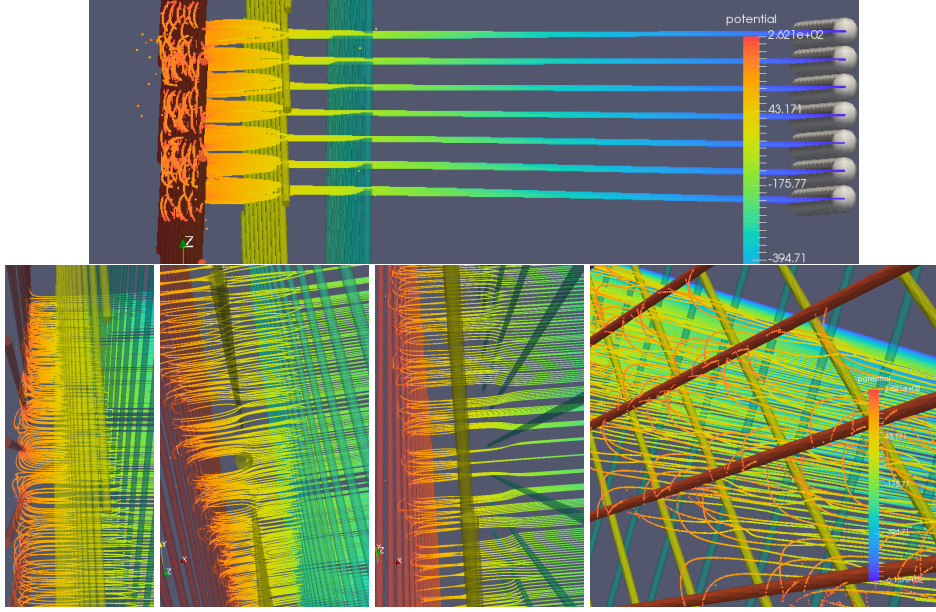
Regardless of the method employed to solve the Laplace equation in 3D, there are various technical computing challenges related to the increase in the size of the resulting field response data set compared to that from 2D calculations. For example, the equivalent of defining a 1D linear grid of six drift path starting points as illustrated in figure 3 is to calculate paths starting on some 2D planar grid. Continuing to require discrete translational symmetry reduces the problem substantially. The minimum set of unique drift paths on the MicroBooNE wire crossing pattern (a hexagonal lattice) is an order of magnitude larger than the 1D linear grid case. For each drift path, one must still calculate one field response function for each wire within range for each plane. The simulation must convolve the drifting charge distributions now in 3D partly by doing a 2D interpolation to the nearest drift paths.

Figure 32 illustrates one possible grid which spans about four times the minimum triangle and has roughly 0.1 mm spacing. Detectors lacking the symmetry of the MicroBooNE wire crossing pattern will require a much larger minimum region. To model a region that lacks translational symmetry requires calculating a family of drift paths which span the entire region. Figure 33 shows an example family of drift paths somewhat equivalent to those shown in figure 2a but calculated in 3D using the BEM.



**Figure 32:** A region of starting points for electron drift paths given a 3D model for MicroBooNE. Blue wires are in the U plane, red are in the Y plane. Potential starting points are represented by white balls. In this example, their separation is roughly 0.1 mm and they span a region about four times as large as the absolute minimum given the wire crossing symmetry.

In addition to the residual discrepancy between the 2D approximation and the real 3D case, the current 2D Garfield calculation has limitations due to its own configuration. Close proximity of the cathode to the wire planes (in our calculation the cathode is 20 cm from the V plane) results in a squeezing of the weighting potential. The effect of this squeezing is most pronounced on the U plane, which has no shielding. Nevertheless, this squeezing effect is only considerable in the case of a long track at small  $\theta_{xz}$ . In this circumstance, the field response from a larger range of wires



**Figure 33:** Various views of a family of possible drift paths through a 3D model of MicroBooNE wires. Paths are colored based on the local electrostatic potential. Path starting points are shown as white balls. Red wires make up the collection plane. The top image shows a view looking approximately across the detector, perpendicular to the collection wires. The bottom row shows views, in order of left to right: along a Y, V and U wire. The final view on the bottom is from behind the wire planes.

(greater than the  $0 \pm 10$  wire in the current calculation) is required because the coherent summation of long-range induction from distant wires is non-negligible.

A dedicated test-stand to calibrate the single-phase LArTPC field response to a point source charge would greatly aid in validating the residual 3D effect to a 2D field response calculation.

## 5.2 Limitations of the current ROI finding

ROI finding is a critical step in charge extraction and has direct consequences for charge bias and inefficiency. For the induction planes, a prolonged (large  $\theta_{xz}$ ) track will have a large bias and inefficiency in charge extraction. An example of such a track is presented in figure 34. The ROI failure occurs on the U plane. The V and Y planes provide an indication of how the topology should have been reconstructed in the U plane view. Given that these highly inclined tracks are extended in time and have small amplitude, the associated ROIs tend not to be found. This effect is more serious at large  $\theta_{xz}$  and for tracks with long drift time, where the effects of diffusion further reduce the amplitude. For short drifting distance with small diffusion, ROI finding for large angle tracks has found some success. Figures 35 and 36 demonstrate the successful recovery of a large  $\theta_{xz}$ , time prolonged signal on the U plane. In the raw data waveform after noise filtering, notice that the signal is buried within the resolution of the baseline. In this case, the 2D deconvolution procedure excels at extracting this low amplitude signal from noise. This example also highlights the intra- and inter-wire dependence of the weighting field on the signal shape, which is quasi-triangular as

discussed in section 4.3.5. A web-based interactive tool to explore the raw waveform, waveform after noise filtering, and the charge spectra after deconvolution can be found in [49].

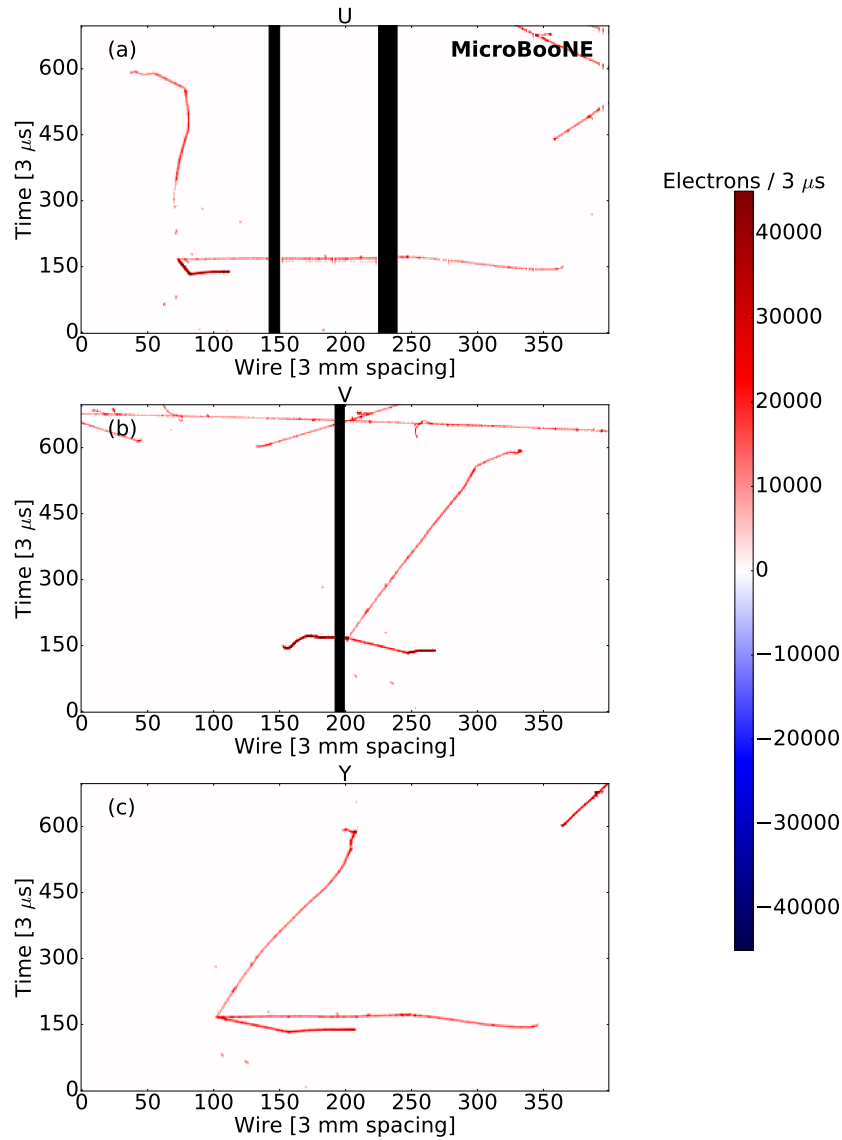


**Figure 34:** An example topology from MicroBooNE data (event 31, run 5366) for which the signal processing failed to find an ROI on the U plane. The signal after 2D deconvolution is displayed. Black rectangles denote inactive TPC wires. (a) U plane view. (b) V plane view. (c) Y plane view

At present, the ROI finding considers the amplitude of the deconvolved signal compared with a certain predefined noise threshold as well as the connectivity of the ROI windows in wire and time dimensions. However, the shape of the reconstructed charge distribution may be helpful to predict or extrapolate the ROI window to fully cover the signal range, and the start drifting position would be used to deconvolve the corresponding diffusion smearing. An adaptive ROI finding threshold would be useful to balance the noise level and charge extraction efficacy. In short, a second-pass signal processing may be attempted with more knowledge of the charge deposition that

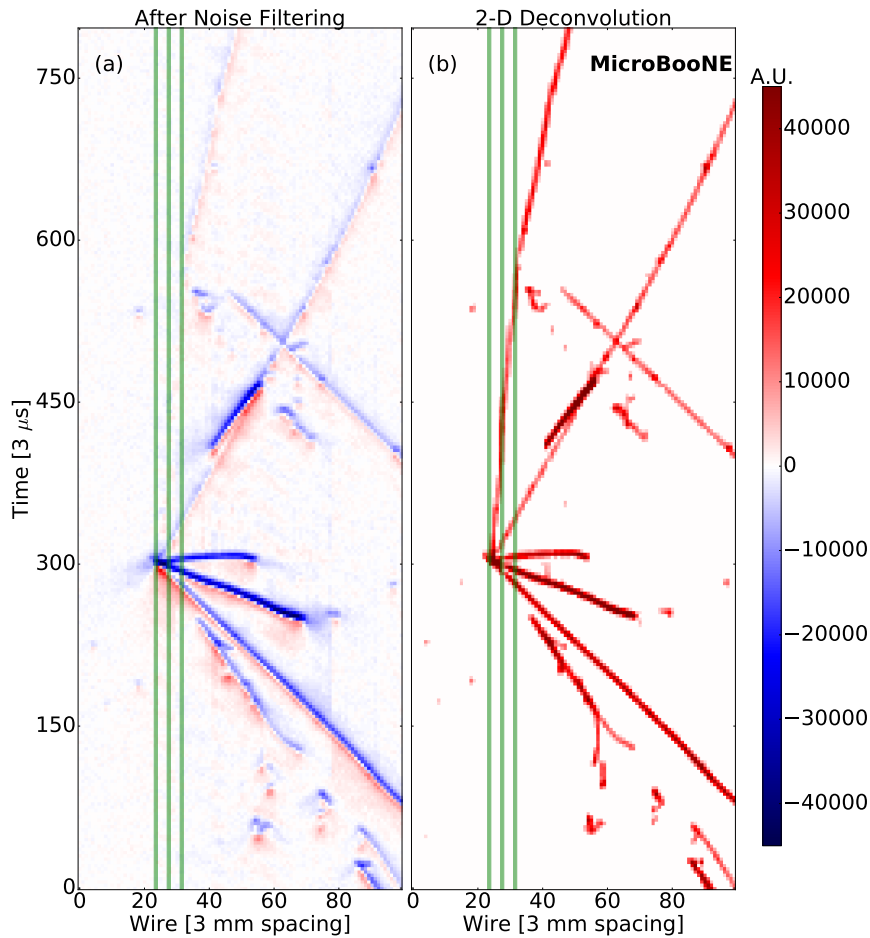


**Figure 35:** A neutrino candidate from MicroBooNE data (event 41075, event 3493) measured on the U plane after (a) noise filtering (in units of average baseline subtracted ADC scaled by 250 per  $3 \mu\text{s}$ ) and (b) 2D deconvolution (in units of electrons per  $3 \mu\text{s}$ ). The vertical green lines denote the wires corresponding to the waveforms and charge spectra, respectively, in figure 36.

can only be obtained after downstream event reconstruction, e.g., start time matching, 3D object matching/imaging, clustering, tracking, etc. These considerations are the subject of ongoing work.

### 5.3 Impact of excess noise in real data

Excess noise, as introduced in [27], can be characterized and largely removed by noise filtering prior to signal processing. However, the noise filter changes the noise spectrum as well as the signal spectrum. For the MicroBooNE detector, the coherent noise removal in the noise filter has a large impact on signal processing. The coherent noise originates from a low-voltage regulator which



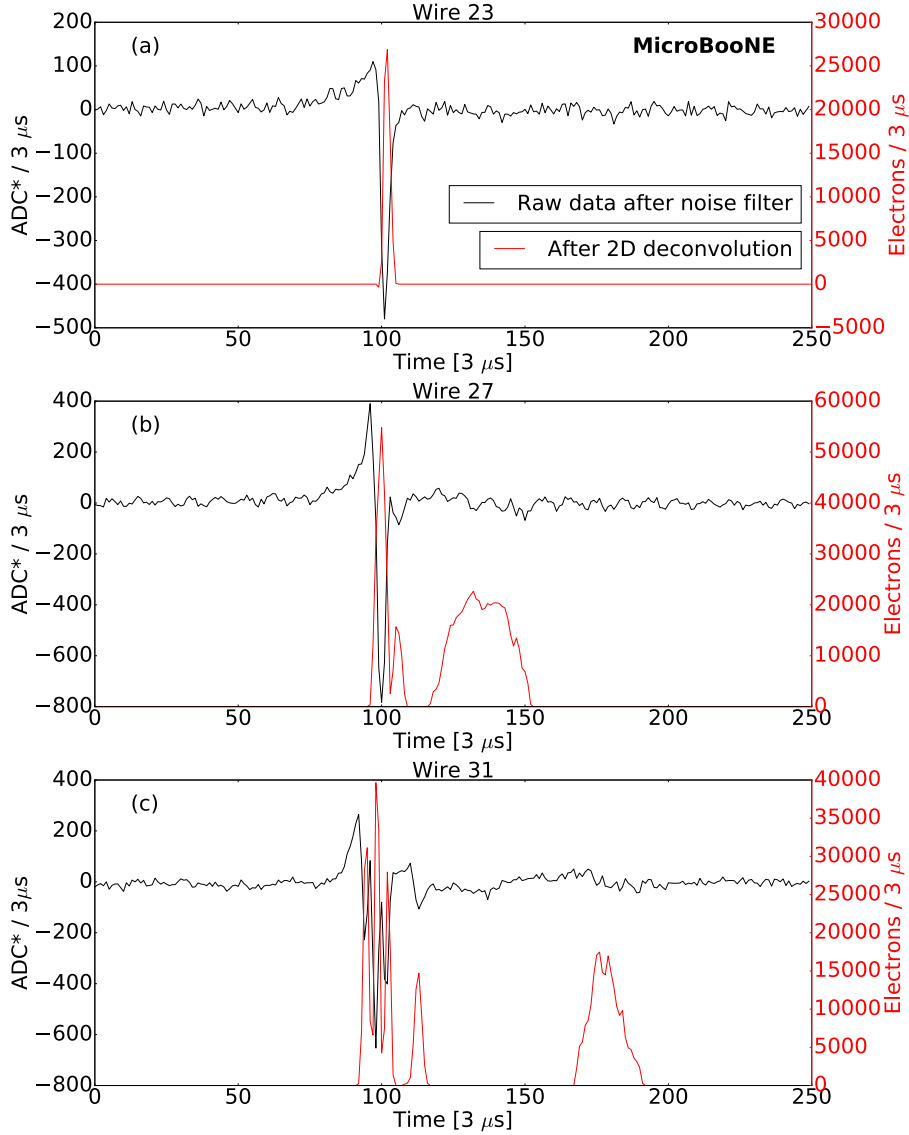


**Figure 36:** Noise-filtered waveforms (black, in units of average baseline subtracted ADC per  $3 \mu\text{s}$ ) and charge spectra (red, in units of electrons per  $3 \mu\text{s}$ ) corresponding to a U plane track with  $\theta_{xz} \approx 84^\circ$ . Note, the quasi-triangular shaped reconstructed signal from the large-angle track. This signal is indistinguishable from the baseline in the noise-filtered waveform.

serves a number of channels/wires and manifests itself at the low end of the frequency spectrum, e.g.  $\leq 30 \text{ kHz}$ . For an isochronous track, the noise filter can mistake the signal as part of the coherent noise and distort the waveforms from a range of wires/channels. Unfortunately, signals from the induction plane, particularly the U plane, are especially affected and have a large fraction of the power spectrum interfered with by the coherent noise. This gives rise to an additional bias for the reconstructed charge for the U plane, a -10 to -20% effect. As the angle of the track increases with respect to the wire plane, this effect is mitigated dramatically, and can typically be ignored for tracks with angle greater than  $5^\circ$ .

## 6 Summary

This paper presents the principle of single phase LArTPC signal formation and a method to perform ionization electron signal analysis and processing for wire readout schemes. Several components of the signal processing are described. Most notably, the implementation of a 2D deconvolution (in time and wire dimensions) is introduced as a natural complement to the field ranges and contours inherent to LArTPC signals. Also, the careful selection and refinement of signal regions of interest are emphasized for a successful extraction of the charge distribution from all sense wire planes.

A full TPC signal simulation with long-range and fine-grained field responses has been developed and employed to evaluate the signal processing. Also, an analytic method has been introduced to simulate inherent electronics noise, which is a driving factor in signal processing performance. This motivates the design decision to develop and employ cold electronics [25] for LArTPC applications.

With the signal and noise simulation, a quantitative assessment of the signal processing method has been performed. For track-like topologies, the signal processing for the collection plane achieved better than 5 % charge resolution, full efficiency, and negligible charge bias for track angle  $\theta_{xz} \lesssim 80^\circ$ ; the signal processing for the induction plane achieved better than 10 % charge resolution, full efficiency, and negligible charge bias with  $\theta_{xz} \lesssim 40^\circ$ . For the induction planes, both the charge bias and charge resolution increase significantly with an increase of track angle  $\theta_{xz}$  greater than  $40^\circ$ . The signal processing has a significant increase in inefficiencies/failures for induction plane tracks with  $\theta_{xz} \gtrsim 75^\circ$ . The simulation is meant not only for the evaluation of signal processing but also as a fundamental tool to understand the LArTPC detector by comparison with real data. The data-to-simulation comparison will be demonstrated in a forthcoming paper [19].

Weak points of the current signal processing method are also presented. These shortcomings are strongly dependent on signal topology. Improvements to these deficiencies are informed by the full chain of event reconstruction and are an active area of development.

Signal processing is the foundation of LArTPC event reconstruction paradigms such as Pandora multi-algorithm pattern recognition [8], deep learning with convolutional neural networks [9], Wire-Cell tomography [11], and therefore the foundation of physics analyses. We present a procedure to extract signal from all planes, taking special precautions to counteract difficult circumstances innate to the induction plane signal. This technique makes a more robust input to the subsequent 3D reconstruction. The signal processing method outlined here brings closer the realization of the promised capability of LArTPC detector technology.

## Acknowledgments

This document was prepared by the MicroBooNE collaboration using the resources of the Fermi National Accelerator Laboratory (Fermilab), a U.S. Department of Energy, Office of Science, HEP User Facility. Fermilab is managed by Fermi Research Alliance, LLC (FRA), acting under Contract No. DE-AC02-07CH11359. MicroBooNE is supported by the following: the U.S. Department of Energy, Office of Science, Offices of High Energy Physics and Nuclear Physics; the U.S. National Science Foundation; the Swiss National Science Foundation; the Science and Technology Facilities Council of the United Kingdom; and The Royal Society (United Kingdom). Additional support for

the laser calibration system and cosmic ray tagger was provided by the Albert Einstein Center for Fundamental Physics, Bern, Switzerland.

## References

- [1] C. Rubbia, *The Liquid Argon Time Projection Chamber: A New Concept for Neutrino Detectors*, CERN-EP-INT-77-08 (1977).
- [2] H. H. Chen, P. E. Condon, B. C. Barish and F. J. Sciulli, *A Neutrino detector sensitive to rare processes. I. A Study of neutrino electron reactions*, FERMILAB-PROPOSAL-0496 (1976).
- [3] W. J. Willis and V. Radeka, *Liquid Argon Ionization Chambers as Total Absorption Detectors*, *Nucl. Instrum. Meth.* **120** (1974) 221.
- [4] D. R. Nygren, *The Time Projection Chamber: A New 4 pi Detector for Charged Particles*, *eConf C740805* (1974) 58 [PEP-0144].
- [5] Y. Li et al., *Measurement of Longitudinal Electron Diffusion in Liquid Argon*, *Nucl. Instrum. Meth. A* **816** (2016) 160, [arXiv:1508.07059].
- [6] LAr1-ND, ICARUS-WA104, MICROBooNE collaboration, M. Antonello et al., *A Proposal for a Three Detector Short-Baseline Neutrino Oscillation Program in the Fermilab Booster Neutrino Beam*, arXiv:1503.01520.
- [7] DUNE collaboration, R. Acciarri et al., *Long-Baseline Neutrino Facility (LBNF) and Deep Underground Neutrino Experiment (DUNE)*, arXiv:1512.06148.
- [8] MICROBooNE collaboration, R. Acciari et al., *The Pandora multi-algorithm approach to automated pattern recognition of cosmic-ray muon and neutrino events in the MicroBooNE detector*, *Eur. Phys. J. C* **78** (2018) 82, [arXiv:1708.03135].
- [9] MICROBooNE collaboration, R. Acciarri et al., *Convolutional neural networks applied to neutrino events in a liquid argon time projection chamber*, *JINST* **12** (2017) P03011, [arXiv:1611.05531].
- [10] MICROBooNE collaboration, P. Abratenko et al., *Determination of muon momentum in the MicroBooNE LArTPC using an improved model of multiple Coulomb scattering*, *JINST* **12** (2017) P10010, [arXiv:1703.06187].
- [11] C. Zhang, X. Qian, B. Viren and M. Diwan, *Three-dimensional Imaging for Large LArTPCs*, arXiv:1803.04850.
- [12] MICROBooNE collaboration, R. Acciarri et al., *Design and Construction of the MicroBooNE Detector*, *JINST* **12** (2017) P07010, [arXiv:1612.05824].
- [13] MINIBooNE collaboration, A. Aguilar-Arevalo et al., *The Neutrino Flux prediction at MiniBooNE*, *Phys. Rev. D* **79** (2009) 072002, [arXiv:0806.1449].
- [14] P. Adamson et al., *The NuMI Neutrino Beam*, *Nucl. Instrum. Meth. A* **806** (2016) 279, [arXiv:1507.06690].
- [15] R. Acciarri et al., *Construction and Assembly of the Wire Planes for the MicroBooNE Time Projection Chamber*, *JINST* **12** (2017) T03003, [arXiv:1609.06169].
- [16] J. Conrad et al., *The Photomultiplier Tube Calibration System of the MicroBooNE Experiment*, *JINST* **10** (2015) T06001, [arXiv:1502.04159].
- [17] O. Bunemann, T. Cranshaw and J. Harvey, *Design of grid ionization chambers*, *Can. J. Research* **Vol: 27A** (1949) .

- [18] J. Asaadi et al., *First Demonstration of a Pixelated Charge Readout for Single-Phase Liquid Argon Time Projection Chambers*, [arXiv:1801.08884](#).
- [19] MICROBooNE collaboration, C. Adams et al., *Ionization Electron Signal Processing in Single Phase LArTPCs II. Data/Simulation Comparison and Performance in MicroBooNE*, [arXiv:1804.02583](#).
- [20] S. Ramo, *Currents Induced by Electron Motion*, *Proceedings of the IRE* **27** (1939) 584.
- [21] C. Cavalleri, E. Gatti, G. Fabri and V. Svelto, *Extension of ramo's theorem as applied to induced charge in semiconductor detectors*, *Nucl. Instrum. Meth.* **92** (1971) 137.
- [22] L. A. Hamel and M. Julien, *Generalized demonstration of ramo's theorem with space charge and polarization effects*, *Nucl. Instrum. Meth. A* **597** (2008) 207.
- [23] R. Veenhof, *GARFIELD, recent developments*, *Nucl. Instrum. Meth. A* **419** (1998) 726.
- [24] Liquid Argon Properties (Tables and Calculators), <http://lar.bnl.gov/properties>, (accessed January 1, 2018).
- [25] V. Radeka et al., *Cold Electronics for "Giant" Liquid Argon Time Projection Chambers*, *J. Phys. Conf. Ser.* **308** (2011) 012021.
- [26] H. Nyquist, *Thermal Agitation of Electric Charge in Conductors*, *Phys. Rev.* **32** (1928) 110.
- [27] MICROBooNE collaboration, R. Acciarri et al., *Noise Characterization and Filtering in the MicroBooNE Liquid Argon TPC*, *JINST* **12** (2017) P08003, [[arXiv:1705.07341](#)].
- [28] G. De Geronimo et al., *Front-end ASIC for a Liquid Argon TPC*, *IEEE Transactions on Nuclear Science* **58** (2011) 1376.
- [29] R. Sulej on behalf of ICARUS collaboration, private communications, 2013.
- [30] B. Baller, *Liquid Argon TPC Signal Formation, Signal Processing and Hit Reconstruction*, *JINST* **12** (2017) P07010, [[arXiv:1703.04024](#)].
- [31] W. Tang et al., *Data Unfolding with Wiener-SVD Method*, *JINST* **12** (2017) P10002, [[arXiv:1705.03568](#)].
- [32] N. Wiener, *Extrapolation, Interpolation, and Smoothing of Stationary Time Series*. The MIT Press, 1964.
- [33] Wire Cell signal processing including noise removal, <https://github.com/WireCell/wire-cell-sigproc>, (accessed January 1, 2018, code version: 0.6.2).
- [34] LArSoft, <http://larsoft.org>, (accessed January 1, 2018).
- [35] GEANT4 collaboration, S. Agostinelli et al., *GEANT4 – a simulation toolkit*, *Nucl. Instrum. Meth. A* **506** (2003) 250.
- [36] T. Doke et al., *Estimation of Fano factors in liquid argon, krypton, xenon and xenon-doped liquid argon*, *Nucl. Instrum. Meth.* **134** (1976) 353.
- [37] M. Jaskolski and M. Wojcik, *Electron Recombination in Ionized Liquid Argon: A Computational Approach Based on Realistic Models of Electron Transport and Reactions*, *J. Phys. Chem. A* **115**(17) (2011) 4317.
- [38] J. Sowada, U. Warman and M. Haas, *Hot-electron thermalization in solid and liquid argon, krypton, and xenon*, *Phys. Rev. B* **25** (1982) 3434(R).
- [39] ARGONeUT collaboration, R. Acciarri et al., *A study of electron recombination using highly ionizing particles in the ArgoNeuT Liquid Argon TPC*, *JINST* **8** (2013) P08005.

- [40] MicroBooNE collaboration, M. Mooney, *The MicroBooNE Experiment and the Impact of Space Charge Effects*, [arXiv:1511.01563](https://arxiv.org/abs/1511.01563).
- [41] M. Diwan. *Basic mathematics of random noise part 1/2*, . Yale University Wright Laboratory Nuclear Particle Astrophysics/Weak Interaction Discussion Group joint seminar, September 19/22, 2017.
- [42] W. Jung, *Op amp application handbook*, Newnes/Elsevier, ISBN-0-7506-7844-5 (2005) .
- [43] A. Pullia and S. Riboldi, *Time-domain simulation of electronic noises*, *IEEE Transactions on Nuclear Science* **51** (2004) 1817–1823.
- [44] R. Moghimi. *Noise Optimization in Sensor Signal Conditioning Circuits [Part 1]*, . <http://www.analog.com/en/education/education-library/webcasts/noise-optim-sensor-sig-condi-p1.html>, 2017.
- [45] L. Rayleigh, *The problem of the random walk*, *Nature* **72** (1905) 294; 318–342.
- [46] MicroBooNE collaboration, R. Acciari et al., *Measurement of cosmic-ray reconstruction efficiencies in the MicroBooNE LArTPC using a small external cosmic-ray counter*, *JINST* **12** (2017) P12030, [[arXiv:1707.09903](https://arxiv.org/abs/1707.09903)].
- [47] C. Brebbia, *The birth of the boundary element method from conception to application*, *Engineering Analysis with Boundary Elements* **77** (2017) iii–x.
- [48] W. Śmigaj et al., *Solving Boundary Integral Problems with BEM++*, *ACM Trans. Math. Software* **41** (2015) 6:1–6:40.
- [49] Magnify Online, <http://lar.bnl.gov/magnify/#/>, (accessed January 1, 2018).